NEUROSCIENCE

Neurodevelopmental defects and neurodegenerative phenotypes in human brain organoids carrying Parkinson's disease-linked *DNAJC6* mutations

Noviana Wulansari[1,2,3]*, Wahyu Handoko Wibowo Darsono[1,2,3]*, Hye-Ji Woo[1,2,3], Mi-Yoon Chang[1,2,3], Jinil Kim[1,2,3], Eun-Jin Bae[4], Woong Sun[5], Ju-Hyun Lee[5], Il-Joo Cho[6,7,8,9], Hyogeun Shin[6,7], Seung-Jae Lee[4†], Sang-Hun Lee[1,2,3†]

Copyright © 2021 The Authors, some rights reserved; exclusive licensee American Association for the Advancement of Science. No claim to original U.S. Government Works. Distributed under a Creative Commons Attribution NonCommercial License 4.0 (CC BY-NC).

Loss-of-function mutations of *DNAJC6*, encoding HSP40 auxilin, have recently been identified in patients with early-onset Parkinson's disease (PD). To study the roles of DNAJC6 in PD pathogenesis, we used human embryonic stem cells with CRISPR-Cas9–mediated gene editing. Here, we show that *DNAJC6* mutations cause key PD pathologic features, i.e., midbrain-type dopamine (mDA) neuron degeneration, pathologic α-synuclein aggregation, increase of intrinsic neuronal firing frequency, and mitochondrial and lysosomal dysfunctions in human midbrain-like organoids (hMLOs). In addition, neurodevelopmental defects were also manifested in hMLOs carrying the mutations. Transcriptomic analyses followed by experimental validation revealed that defects in DNAJC6-mediated endocytosis impair the WNT-LMX1A signal during the mDA neuron development. Furthermore, reduced *LMX1A* expression during development caused the generation of vulnerable mDA neurons with the pathologic manifestations. These results suggest that the human model of *DNAJC6*-PD recapitulates disease phenotypes and reveals mechanisms underlying disease pathology, providing a platform for assessing therapeutic interventions.

INTRODUCTION

Parkinson's disease (PD) is a common neurodegenerative disorder characterized by progressive loss of dopamine (DA) neurons in the substantia nigra of the midbrain. Toxic intraneuronal α-synuclein (α-syn) aggregates, mitochondrial dysfunction, defects in vesicular trafficking, and impaired endo-lysosomal degradation underlie PD pathologic features [reviewed in (*1*)]. Genetic research on PD has identified monogenic forms of the disorder and genetic risk factors. Studies on these genetic mutations have expanded our understanding of the disease pathogenesis and help identify the therapeutic targets.

DNAJC6 (DNAJ/HSP40 homolog, subfamily C member 6; MIM 608375) encodes auxilin, which acts as a co-chaperone to recruit HSC70 to clathrin-coated vesicles for disassembly (*2*). Homozygous loss-of-function mutations of *DNAJC6* have been identified in familial juvenile parkinsonism (*3*–*5*). Mice lacking DNAJC6 exhibited a high rate of unexplained early postnatal mortality. Defects in synaptic recycling and Golgi-lysosomal trafficking have been reported in cells derived from *Dnajc6*-Knockout (*Dnajc6*-KO) mice (*3*, *6*). However, the studies using the KO mice have failed to show PD-associated phenotypes, e.g., loss of DA neurons and intraneuronal α-syn inclusions in the substantia nigra. Analysis using samples from the patients and postmortem brains is not realistic, due to the limited number of the patients, all of whom are alive. Thus, the pathogenic mechanism for PD caused by *DNAJC6* mutations remains unclear.

PD is classically considered an age-associated disorder. However, neurodevelopmental aspects might contribute to the PD pathogenesis (*7*). First, exposure of pesticides or brain injury at pre-/perinatal ages leads to dysfunction of the midbrain DA neuron system in adult life (*8*, *9*). In addition, along with roles of many PD-associated genes (i.e., PARK genes) in neuronal developmental processes [reviewed in (*10*)], juvenile forms of PD have been reported in patients with mutations in PARK genes such as *FBXO7*, *ATP13A2*, *SYNJ1*, *PLA2G6*, *DNAJC6*, *PINK1*, and *PRKN* [reviewed in (*11*)]. In particular, all the patients with PD carrying *DNAJC6* mutations are those with juvenile or early disease onset (most of them at ≥ age 10), and defects associated with neurodevelopment (i.e., microcephaly) are detected in patients with *DNAJC6* mutations (*4*). These observations led to the hypothesis that improper midbrain-type DA (mDA) neuron development could have an impact on the viability and resistance to toxic insults of adult mDA neuron.

In the early developing ventral midbrain (VM), Wnt Family Member 1 (WNT1), and Fibroblast Growth Factor 8 (FGF8), secreted from the isthmic organizer, establish the expression of the transcription factor *LMX1A* in the earliest mDA neuron precursor cells, while *FOXA2* is expressed by the action of Sonic Hedgehog (SHH) secreted from the floor plate (*12*–*14*). The developmental factors FOXA2 and LMX1A act together as master regulators and induce the expression of a battery of later-development genes such as *NURR1* (*NR4A2*), *PITX3*, and *NEUROGENIN 2* (*NGN2*). These early and late genes interact with each other in a feed-forward manner in the later stages of developing VM (*15*–*17*). The early-development [*LMX1A*, *FOXA2*, and *ENGRAILED-1*, *2*

[1]Department of Biochemistry and Molecular Biology, College of Medicine, Hanyang University, Seoul, Republic of Korea. [2]Hanyang Biomedical Research Institute, Hanyang University, Seoul, Republic of Korea. [3]Graduate School of Biomedical Science and Engineering, Hanyang University, Seoul, Republic of Korea. [4]Department of Biomedical Sciences and Medicine, Neuroscience Research Institute, Seoul National University College of Medicine, Seoul, Republic of Korea. [5]Department of Anatomy, Brain Korea 21 PLUS Program for Biomedical Science, Korea University College of Medicine, Seoul 02841, Republic of Korea. [6]Center for BioMicrosystems, Brain Science Institute, Korea Institute of Science and Technology, Seoul, Republic of Korea. [7]Division of Bio-Medical Science and Technology, KIST School, Korea University of Science and Technology, Daejeon, Republic of Korea. [8]School of Electrical and Electronics Engineering, Yonsei University, Seoul 03722, Republic of Korea. [9]Yonsei-KIST Convergence Research Institute, Yonsei University, Seoul 03722, Republic of Korea.
*These authors contributed equally to this work.
†Corresponding author. Email: leesh@hanyang.ac.kr (S.-H.L.); sjlee66@snu.ac.kr (S.-J.L.)

(*EN1/2*)] and late-development (*NURR1* and *PITX3*) genes continue to be expressed in mDA neurons of adult midbrain, and their expression is critical for cell viability of adult mDA neurons and prevention of neurodegeneration (*18*–*20*). LMX1A and its homolog, LMX1B, exert their roles in the regulation of mitochondrial function (*21*) and the autolysosomal process (*22*), thereby supporting the survival of mDA neurons. EN1/2 protect the mDA neurons from oxidative stress through increasing mitochondrial complex I activity and regulating DNA damage response and chromatin remodeling (*20*, *23*). NURR1 is also involved in mitochondrial biogenesis by activating mitochondrial gene transcriptions (*24*), while negatively regulating α-syn transcription (*25*). Possible genetic links between these midbrain-specific factors and PD have been reported (*26*, *27*).

In this study, to elucidate the mode of action of *DNAJC6* mutations in PD pathogenesis, we established isogenic human embryonic stem cells (hESCs), in which deleterious *DNAJC6* mutations were inserted using CRISPR-Cas9–mediated gene editing. First, we showed that human midbrain-like organoids (hMLOs) and mDA neurons derived from the hESCs harboring *DNAJC6* mutations are useful human disease models clearly exhibiting key PD pathologic features, such as mDA neuron degeneration and α-syn aggregation. Further analyses of these models identified the WNT-LMX1A autoregulatory pathway as being impaired during the early developmental period of hMLOs carrying DNAJC6 mutations. Our human model suggests that the impaired developmental signaling is the major driver yielding disease-susceptible mDA neurons.

RESULTS

Generation of an isogenic hESC-based human disease model to assess the pathogenic role of *DNAJC6* mutation in PD

DNAJC6 gene mutations in patients with PD are associated with homozygous mutations that cause a loss of gene function. To create an in vitro human disease model to assess the pathogenic role of DNAJC6 in PD, we generated a homozygous *DNAJC6* ablation in hESCs using CRISPR-Cas9 with a single-guide RNA (sgRNA) that targets the *DNAJC6* gene locus, which spans intron 6 to exon 7. The sgRNA was made by mimicking the gene mutation (c.801-2 A → G) reported in familial PD, which causes gene expression loss due to mRNA instability (*3*). After cotransfecting hESCs (H9) with a plasmid-encoding Cas9 and the sgRNA, colonies derived from a single cell were obtained and expanded with serial passages (fig. S1A). Among those derived from the colonies, three cell lines harboring biallelic (homozygous) mutations were chosen for analysis, with three unedited wild-type (WT) hESCs derived from the colonies that underwent the same CRISPR-Cas9 reactions but without the sgRNA (Fig. 1A and fig. S1, B and C). Consistent with the findings of Edvardson *et al.* (*3*), the mutants showed *DNAJC6* mRNA instability (Fig. 1B) possibly by nonsense-mediated mRNA decay (NMD) (*28*), which ultimately led to reduced mRNA and protein expression (Fig. 1, C to E). However, decreased DNAJC6 expression did not alter the hESC properties such as pluripotent-marker expression, cell growth, self-renewal, or survival of hESCs (fig. S2, A to D).

Early ventral midbrain patterning defects by deleterious *DNAJC6* mutation

To investigate the role of *DNAJC6* mutation in PD pathogenesis, we induced differentiation of mutant and WT hESC lines toward hMLOs that resemble the developing VM, which is the region of the brain that is primarily affected in PD (Fig. 1F and fig. S3A). At differentiation day 15 [DIV (days in vitro)15], hMLOs differentiated from the WT-hESCs contained numerous $PLZF^+$ or $SOX2^+$ neuroepithelial rosette (neural tube) structures, characterized by apico-basal polarity with ZO-1, ZO-2, N-CADHERIN, and OCLUDIN expression at the apical side (fig. S3, C to E). The rosettes were stained with the markers for general neural stem/precursor (NESTIN), anterior embryonic brain (OTX2), embryonic midbrain (EN1), and VM floor-plate cells (FOXA2 and LMX1A) (Fig. 1, G, H, J, and L, and fig. S3F), indicating that the organoids were correctly patterned into the VM-type embryonic brain region, which is composed largely of undifferentiated neural stem/precursor cells (NSCs). It is of note that the neural tube structures were less intact in the mutant hMLOs than WT hMLOs (fig. S3, C to F), along with decreased apical OCLUDIN expression (fig. S3E), which is controlled by canonical WNT signaling (*29*). Furthermore, the expression of LMX1A and EN1 from the early stage of mutant hMLOs (DIV15) was markedly reduced (Fig. 1, G and J to M). LMX1A, together with FOXA2, acts as a master regulator for mDA neuron development in the developing VM by inducing expression of a battery of later-development genes, such as *NURR1*, *PITX3*, and *NGN2*, and interacting with them in a feed-forward manner to induce mDA neuron generation (*15*–*17*). Consistently, the expression of the later-development gene *NURR1* was reduced in mutant hMLOs at a later differentiation day (DIV30) (Fig. 1, G, N, and O).

In addition to the organoid culture, we used NSC culture isolated from the early VM-patterned hMLOs (Fig. 1F and fig. S3B). The hMLO-derived NSC culture is uniform with respect to the expression of a set of VM-NSC–specific markers and can be readily induced to differentiate toward authentic mDA neurons expressing midbrain-specific markers in a pattern similar to mDA neuron development in the developing midbrain (fig. S3B). On the basis of these properties, we decided to use the NSC culture as a research platform to study the pathogenic mechanisms of PD. When NSCs were derived from the WT hMLOs, they uniformly expressed VM-specific FOXA2 and LMX1A (>95% of total cells). Expression of the later-development gene *NURR1* commenced 3 to 5 days after differentiation induction of the WT NSCs toward mDA neurons (figs. S3B and S4). The decreases of LMX1A, EN1 (expansion; differentiation day 0, D0), and NURR1 expression (D5) were also manifested in the NSCs and differentiating NSCs derived from the mutant hMLOs, respectively (fig. S4, A to I).

To attain a molecular insight into the developmental defects mediated by DNAJC6 ablation, we analyzed the global transcriptomes of the mutant and WT organoids over the time points during hESC-hMLO differentiation. Analyses with unsupervised hierarchical clustering have revealed that transcriptomes of the WT hMLOs and the mutant hMLOs were similar at undifferentiated (DIV0) and early hMLO culture days (DIV4) but became segregated from each other by DIV15 (Fig. 1P). Consistently, Gene Ontology (GO) and Kyoto Encyclopedia of Genes and Genomes (KEGG) analyses have shown that genes down-regulated in mutant hMLOs (versus WT hMLOs) at DIV15 were enriched in the ontologies of "midbrain development" and "DA neuron differentiation" (highlighted in green in Fig. 2A). Specifically, down-regulation of the key mDA neuron developmental genes *LMX1A*, *OTX1*, *OTX2*, *EN1*, *EN2*, *NURR1*, *PTX3*, *NGN2*, *ASCL1* (*MASH1*), and *MYT1L* was shown in the RNA sequencing (RNA-seq) data of the mutant hMLOs at DIV15 and DIV30 (Fig. 1, Q and R). The decreased expressions of *LMX1A*, *EN1*, and *NURR1* in all three mutants were further

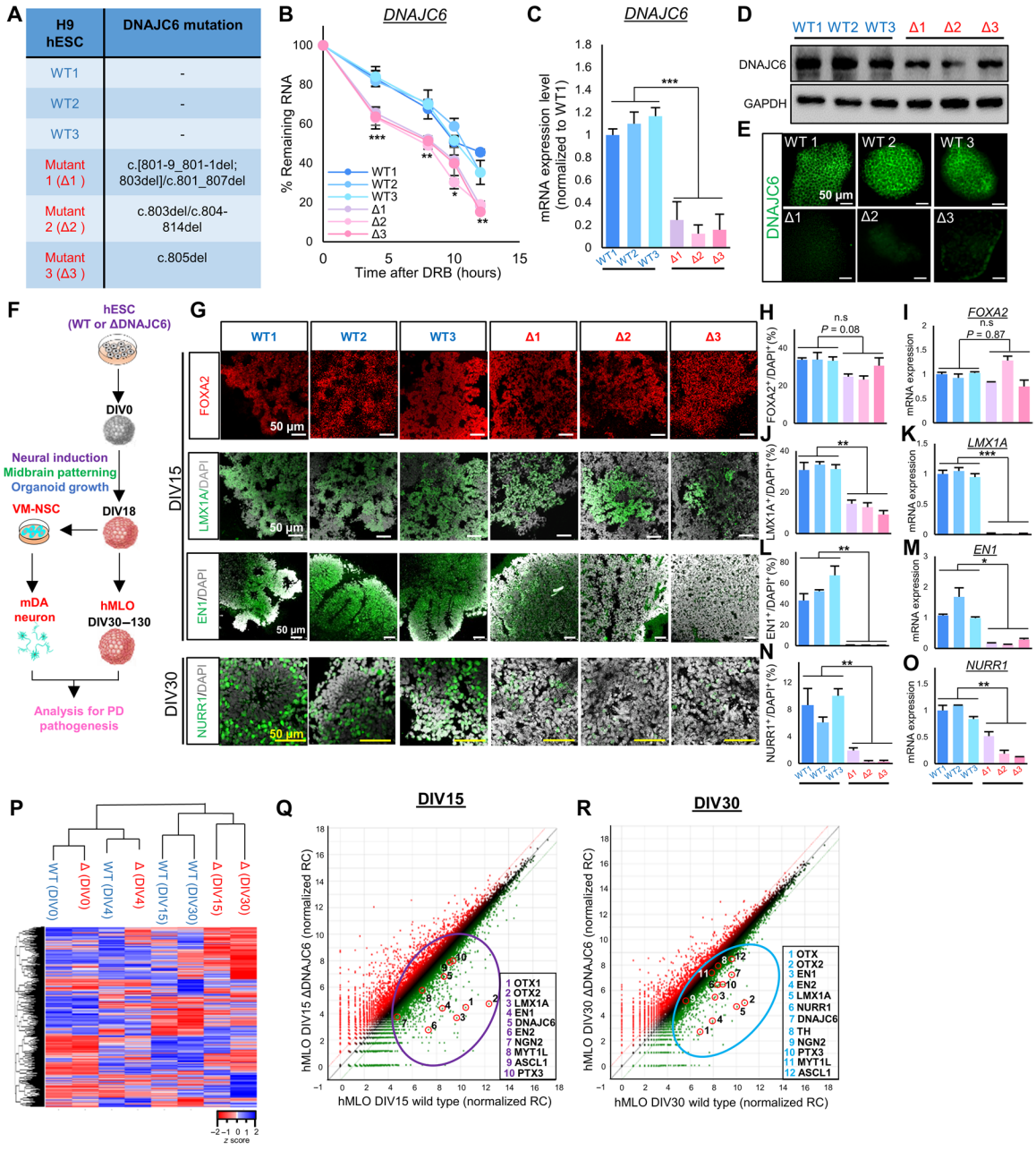

Fig. 1. Ventral midbrain patterning defects in *DNAJC6* mutant human midbrain-like organoids. (**A**) Summary of mutated gene sequences in the *DNAJC6* mutant hESCs (Δ1, 2, 3) generated in our study. (**B**) *DNAJC6* mRNA stability in the WT and mutant hESCs. DRB, 5,6-dichloro-1-beta-D-ribofuranosylbenzimidazole, a mRNA transcription inhibitor. (**C** to **E**) mRNA and protein expressions of *DNAJC6* estimated by quantitative polymerase chain reaction (qPCR) (C), Western blot (WB) (D), and immunocytochemical (E) analyses. Scale bars, 50 μm. (**F**) Schematic of hESCs differentiated to hMLOs, two-dimensional VM neural stem/precursor cells (NSCs), and mDA neuron cultures, used as an experimental platform. (**G** to **O**) Expression of the early (FOXA2, LMX1A, and EN1) and late (NURR1) midbrain-specific markers. The early and late midbrain marker expressions were determined in the WT and mutant hMLOs at DIV15 and DIV30, respectively, using immunocytochemical (G, H, J, L, and N) and qPCR (I, K, M, and O) analyses. For quantification of the marker-positive cells, five hMLOs from five different batches from each WT and mutant cultures were cryosectioned at 16-μm thickness, and the positive cells were counted every five sections from each hMLO. Scale bars, 50 μm. (**P** to **R**) RNA sequencing (RNA-seq) analysis for WT versus mutant hMLO cultures at DIV0, DIV4, DIV15, and DIV30. (P) Unsupervised hierarchical clustering for the differentially expressed genes (DEGs) between the WT and mutant hMLOs [fragments per kilobase of transcript per million mapped reads (FPKM) >1, fold change >2]. (Q and R) Scatterplots of the DEGs highlighting mDA neuron developmental genes are included in the most significantly and greatly up-regulated in the WT hMLOs versus mutant hMLOs at DIV15 and DIV30. Data are presented as means ± SEM, $n = 3$ independent experiments. Significance at $^*P < 0.05$; $^{**}P < 0.01$; $^{***}P < 0.001$, Student's t test; n.s., no significance.

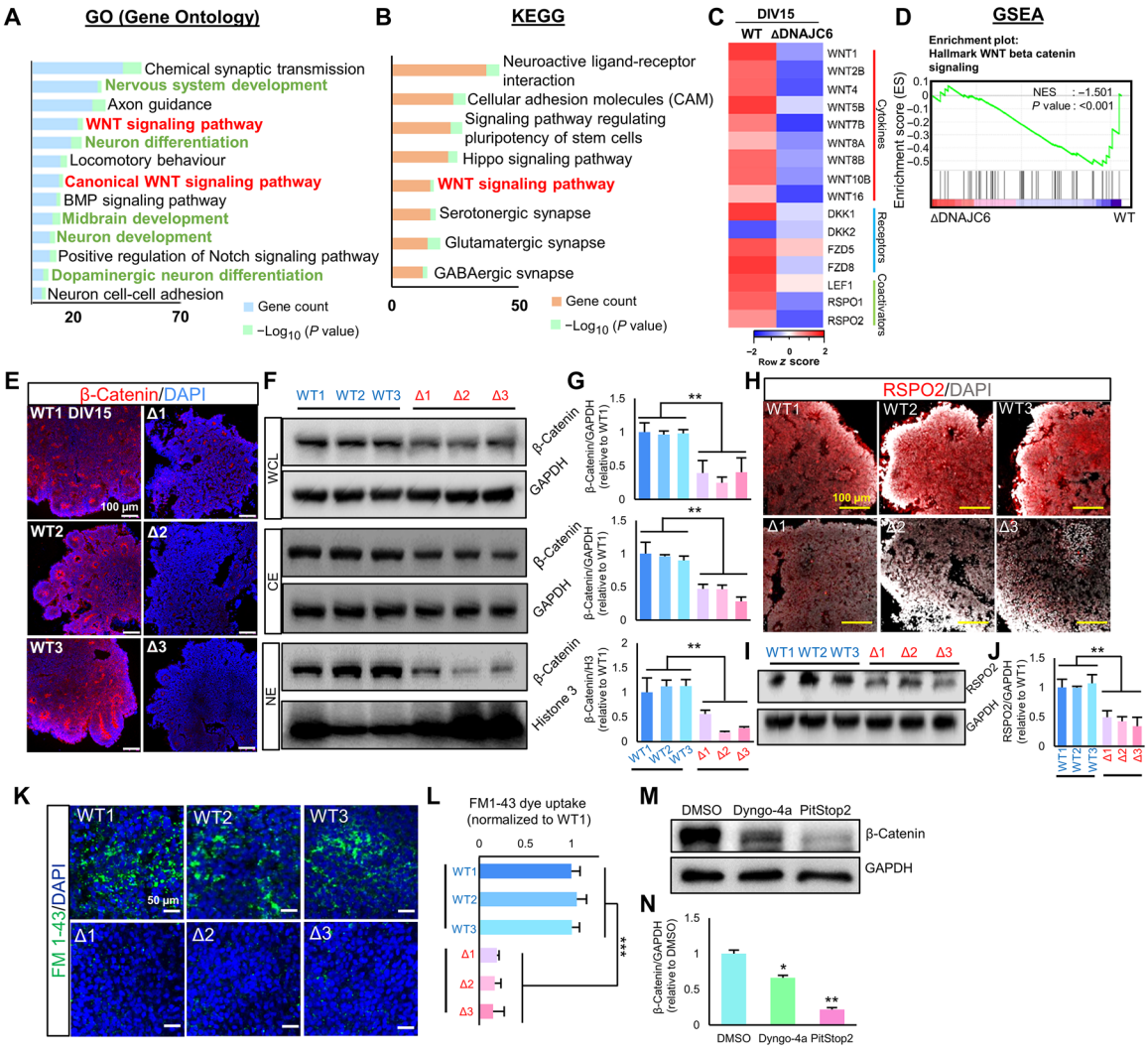

Fig. 2. Loss of DNAJC6-mediated CME causes defects in WNT intracellular signaling at early stages of *DNAJC6* mutant hMLOs. (**A** and **B**) Top GO and KEGG pathways for the genes down-regulated in mutant hMLOs (versus WT hMLOs) at DIV15. "WNT signaling pathway" is highlighted in red. "mDA development"–related categories are highlighted in green. (**C**) Heatmap for the expressions of WNT cytokines, receptors, and coactivators in the RNA-seq data. Expression values are shown as log_2-transformed normalized read counts. (**D**) Gene set enrichment analysis (GSEA) showed enrichment of WNT signaling in WT cells compared with mutant *DNAJC6*. (**E** to **G**) Immunocytochemical (E) and WB analyses (F) to determine β-catenin protein levels in the WT and mutant hMLOs at DIV15. Intensities of the bands in (F) were quantified using ImageJ software, and the values were normalized to glyceraldehyde-3-phosphate dehydrogenase (GAPDH) (G). WCL, whole-cell lysate; CE, cytosolic extract; NE, nuclear extract. Scale bars, 100 μm. (**H** to **J**) Immunocytochemical (H) and WB analyses (I) to determine R-spondin 2 protein levels in the WT and mutant hMLOs at DIV15. Intensities of the bands in (I) were quantified using ImageJ software, and the values were normalized to GAPDH (J). (**K** and **L**) Endocytic capacity assessed by the uptake of FM1-43 dye (K). Fluorescence intensity of FM1-43 was measured using ImageJ in 30 cells randomly chosen from each WT and mutant NSC cultures (L). Scale bars, 50 μm. (**M** and **N**) Decrease of β-catenin protein levels by treatment of the clathrin-mediated endocytosis inhibitor (M). The WB analysis was done in the VM-NSC cultures derived from WT1-hMLOs. Intensities of the bands in (M) were quantified using ImageJ software, and the values were normalized to GAPDH (N). Data are presented as means ± SEM. $n = 3$ independent experiments. DMSO, dimethyl sulfoxide. Significance at $^*P < 0.05$; $^{**}P < 0.01$; $^{***}P < 0.001$, Student's t test (G, J, and L) and two-way analysis of variance (ANOVA) followed by Bonferroni's post hoc test (*M*).

validated by quantitative polymerase chain reaction (qPCR) analysis (Fig. 1, K, M, and O).

Loss of DNAJC6-mediated endocytosis causes defective WNT-LMX1A autoregulation

In RNA-seq data at hMLO DIV15, one of the top categories of the down-regulated genes in the mutant hMLOs (versus the WT hMLOs) was "WNT signaling pathway" (highlighted in red in Fig. 2, A and B), along with reduction of the mRNA levels for WNT cytokines, receptors, and coactivators (Fig. 2C). The enrichment of WNT signaling along with mDA neuron development was further confirmed by gene set enrichment analysis (Fig. 2D). The WNT signaling has been reported to be critical for early mDA neuron development (*30*). The canonical WNT pathway is converged into β-catenin activation and its translocalization to the nucleus, where it acts as an activator to induce T cell factor/lymphoid enhancer-binding factor (TCF/LEF)–mediated gene transcriptions. In immunocytochemical and Western blot (WB) analyses, the protein levels of

β-catenin (especially in the nucleus) were greatly reduced in the mutant hMLOs by DIV15 (Fig. 2, E to G). In addition, down-regulation of R-spondin 2 (RSPO2), coactivator of WNT/β-catenin signaling, which prevents clearance of the Frizzled–low density lipoprotein receptor-related protein (LRP) WNT receptor complex (*31*), was also manifested in mutant hMLOs (Fig. 2, H to J).

The signal activation of WNT is known to require clathrin-mediated endocytosis (CME) of the WNT ligand-receptor complexes [reviewed in (*32*)]. Consistent with the role of DNAJC6 in CME (*2*), endocytic capacity, assessed by the uptake of FM1-43 dye, was clearly decreased in mutant NSC cultures (Fig. 2, K and L). Furthermore, the treatment of the CME inhibitor Dyngo-4a (dynamin inhibitor) and PitStop2 (clathrin inhibitor) in WT NSCs resulted in a decrease in intracellular β-catenin levels (Fig. 2, M and N), collectively indicating that CME impairment caused by loss of DNAJC6 is responsible for the down-regulation of WNT signaling in mutant hMLOs.

LMX1A and *EN1* are potential targets for WNT-β-catenin–mediated transcription (*15*, *33*, *34*). Consistently, along with reduced nuclear levels of β-catenin (Fig. 2, F and G) and down-regulation of *LMX1A* and *EN1* mRNA expression (Fig. 1, K and M), chromatin immunoprecipitation (ChIP) analysis showed lower enrichment of β-catenin proteins bound to the promoter regions of *LMX1A* and *EN1* in mutant NSC cultures (fig. S6, A to D), confirming that decreased expression of *LMX1A* and *EN1* in mutant *DNAJC6* cultures is mediated by impaired canonical WNT-β-catenin signals.

While WNT-β-catenin regulates *LMX1A* and *EN1*, *LMX1A* also activates transcriptions of *WNT* cytokines (*15*, *35*) and *RSPOs* (*36*, *37*). Consistently, along with reduced mRNA levels of *WNT1*, *WNT4*, and *RSPO2* in mutant cultures (Fig. 2C and fig. S6, E to G), forced *LMX1A* expression in the mutant NSCs significantly recovered *WNT* cytokine and *RSPO2* expression (fig. S6H), indicating that a reciprocal transcription activation loop between *LMX1A* and *WNT* is established in early hMLO, similar to early embryonic VM (*15*) and that the positive regulatory pathway is abolished by loss of DNAJC6 function. Together, our findings suggest that loss of DNAJC6-mediated CME causes impaired WNT signaling, WNT-mediated *LMX1A* and *EN1* expression, and ultimately *WNT-LMX1A* positive-feedback regulation, which is critical for early VM patterning and mDA neuron development, in mutant hMLOs.

Early WNT-LMX1A impairment in *DNAJC6* mutants yielded vulnerable mDA neurons without the midbrain-specific factor expression

The decreased expression of *LMX1A* and *EN1* in the early stages of mutant hMLOs might be considered a contributing factor to PD pathogenesis. This postulation was derived from the fact that these genes together with its downstream gene *NURR1* continue to express in adult mDA neurons, and the expression of these midbrain-specific factors in adult mDA neurons is critical for survival and resistance to toxic insults (*18*–*20*). Therefore, the decreased expression of *LMX1A* and *EN1* in early development can yield mDA neurons with reduced dopaminergic identity, thus making them vulnerable to toxic insults.

TH^+ cells were initially scarce, with immature neuronal shapes predominating at early hMLO periods (DIV15 to DIV30). The TH^+ neuronal cells gradually increased during the period of hMLO cultures (fig. S7A) and, consistent with a previous study (*38*), became the majority at DIV50 to DIV70 of the hMLOs (fig. S7, A and B). They also expressed other DA neuron–specific genes *DAT*, *VMAT2*, and *AADC*, confirming DA neuronal phenotypes of the TH^+ cells (fig. S3A). Consistent with the continued expression of mDA neuron developmental genes (*39*), TH^+ DA neurons in late WT hMLOs and differentiated WT-NSC cultures faithfully expressed early (LMX1A and EN1) and late (NURR1) developmental factors (Fig. 3, A to L, and fig. S3, A and B). By contrast, an early deficit of LMX1A expression in the mutant hMLOs (Fig. 1, G, J, and K) resulted in TH^+ DA neurons with lower yields (up to 50% of the WT yields) and with markedly reduced expression of midbrain-specific markers (Fig. 3, A to L). Consistent with the midbrain factors' roles in mDA neuron survival, TH^+ DA neurons in mutant hMLOs exhibited small and shrunken cell bodies with shortened and fragmented neurites, a sign of neuronal cell apoptosis and degeneration (Fig. 3, M and N). Increased apoptotic cells (cleaved caspase-3^+) followed by severe cell death ($EthD1^+$), compared with WTs, were evident in late hMLOs carrying *DNAJC6* mutations (Fig. 3, Q, R, U, and V), resulting in reduction of the mutant hMLO sizes from late-culture periods (fig. S7, C and D). Along with decreased yields and midbrain-specific factor expression in TH^+ cells, increased DA neuron degeneration and cell deaths were manifested in the cultures differentiated from the mutant NSCs (Fig. 3, O, P, S, T, W, and X).

α-Synucleinopathy and stressful pacemaking detected in late hMLOs and mDA neurons carrying *DNAJC6* mutants

Extracellular neuronal recording using a multielectrode array showed an increase in firing frequencies in mutant hMLOs (more than twice that of WT hMLOs) at DIV80 (Fig. 4A and fig. S8, A and B). The increase of intrinsic pacemaker frequency ("stressful pacemaking") is a neuronal characteristic in progressive PD, which is caused by oxidative impairment of A-type Kv4.3 potassium channels (*40*). In addition, low levels of DA neurotransmitters due to defective presynaptic DA release stimulated the intrinsic firing frequency of mDA neurons via D1 receptor stimulation (*41*, *42*). Oxidative stress estimated by dihydrodichlorofluorescein diacetate (DCF), a dye detecting cellular reactive oxygen species (ROS), was much greater in mutant hMLO and differentiated hNSC (mDA neuron) cultures than in WT counterparts (Fig. 4, B and C). In addition, consistent with synaptic vesicle recycling defects with impaired CME in neurons derived from Dnajc6-KO mice [(*6*) and Fig. 2, K and L], significantly lower levels of DA release (especially when evoked by depolarization) were manifested in mutant cultures (Fig. 4D). The decrease of DA release in mutant *DNAJC6* was likely also caused by the decrease in intracellular DA metabolism itself, as the key limiting enzymes for DA production, such as *TH* and *DDC*, are lower in mutant hMLOs (Fig. 4E).

In WB analyses, toxic α-syn oligomers (trimer) were readily detected in the Triton X-100–soluble fractions from mutant hMLOs (Fig. 4, F and G), whereas oligomers were barely detected in WT hMLOs at DIV55. The α-syn pathology in mutant hMLOs was more advanced with the increased formation of high–molecular weight α-syn aggregates in SDS-soluble (Triton X-100–insoluble) fractions at DIV130 (Fig. 4, H and I). In addition to the aggregated forms of this protein, α-syn monomer was also increased in the mutant hMLOs, resulting in a drastic increase of total α-syn protein levels by loss of DNAJC6. Endogenous mRNA expression of α-syn was indistinguishable between the WT and mutant cultures (fig. S8C), collectively indicating a defect in α-syn proteostasis in DNAJC6 mutant hMLOs. Unlike in hMLOs, we were not able to detect the endogenous α-syn in both WT and mutant neurons (fig. S8D). We then further scrutinized the propensity of aggregate formation by

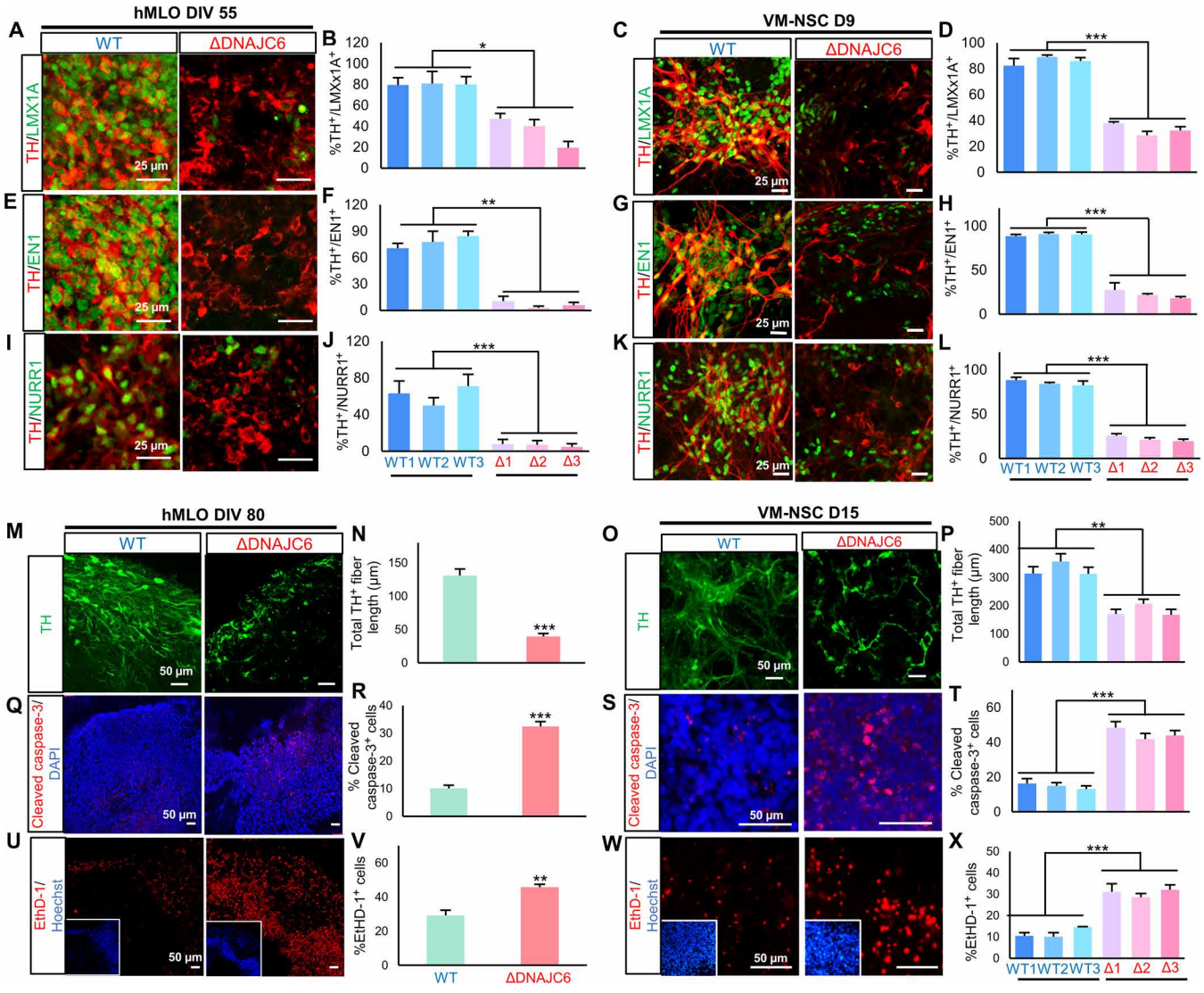

Fig. 3. *DNAJC6* mutations yield DA neurons lacking midbrain-specific factor expression and undergoing degeneration. (**A** to **L**) Midbrain-specific factor expression in DA neurons in late hMLO (A, B, E, F, I, and J) and differentiated NSC cultures (C, D, G, H, K, and L). Images shown are representative and taken from the cultures derived from WT1 and mutant-3. Scale bars, 25 μm. (**M** to **X**) DA neuron degeneration assessed by a morphometric analysis on TH^+ neurons (M to P), % apoptotic cells (cleaved caspase-3^+) (Q to T), and % cell death (EthD-1^+) cells (U to X). Insets in (U) and (W) are Hoechst$^+$ cells. In the morphometric analysis, TH^+ fiber length per DA neuron was estimated in WT and mutant cultures, $n = 3$ biological replicates; in each WT- and mutant-derived culture, 30 TH^+ cells were assessed. Scale bars, 50 μm. Data are presented as means ± SEM, $n = 3$ independent experiments. Significance at $^*P < 0.05$; $^{**}P < 0.01$; $^{***}P < 0.001$, Student's *t* test.

exogenously introduced WT α-syn. Much greater amounts of aggregates were formed from the exogenous α-syn in the mutant neuron (hNSC D12) than those of the WTs (fig. S8D). In addition, we further quantitatively assessed the increased intracellular α-syn oligomerization in the mutant hMLO DIV55 and hNSC D12 by using a bimolecular fluorescence complementation (BiFC) system (*43*), in which intracellular α-syn dimers and oligomers can be detected by yellow fluorescence in cells transfected with α-syn fused to either the amino (N) terminus (V1S) or carboxy (C) terminus (SV2) fragment of Venus, a variant of yellow fluorescence protein (Fig. 4, J to M). Formation of α-syn multimers in the late mutant hMLO cultures was further confirmed by detecting cell populations positive for phosphorylated α-syn at serine 129 (p129-α-syn; pS129), which were double positive for ProteoStat, a dye specific for aggregated proteins (fig. S8E).

Mitochondrial and autolysosomal defects underlie pathologic α-syn accumulation in *DNAJC6* mutant neuronal cells

Mitochondrial dysfunction is a critical feature of PD pathogenesis, contributing to the formation of misfolded α-syn and oxidative stress (*44*). Roles for the midbrain-specific factors LMX1A, EN1, and NURR1 in mitochondrial functions and biogenesis have been shown in mDA neuronal cells (*21*, *23*, *24*). In agreement with these reports, it is highly possible that the mutant mDA neurons with lack of the midbrain factor expressions undergo mitochondrial dysfunctions and impairment. Increased mitochondrial ROS levels (MitoSox; Fig. 5, A and B) were found in mutant mDA neuron cultures. In addition, we found a significant decrease of mitochondrial membrane potentials (JC-1; Fig. 5, D and E), indicating mitochondrial damage.

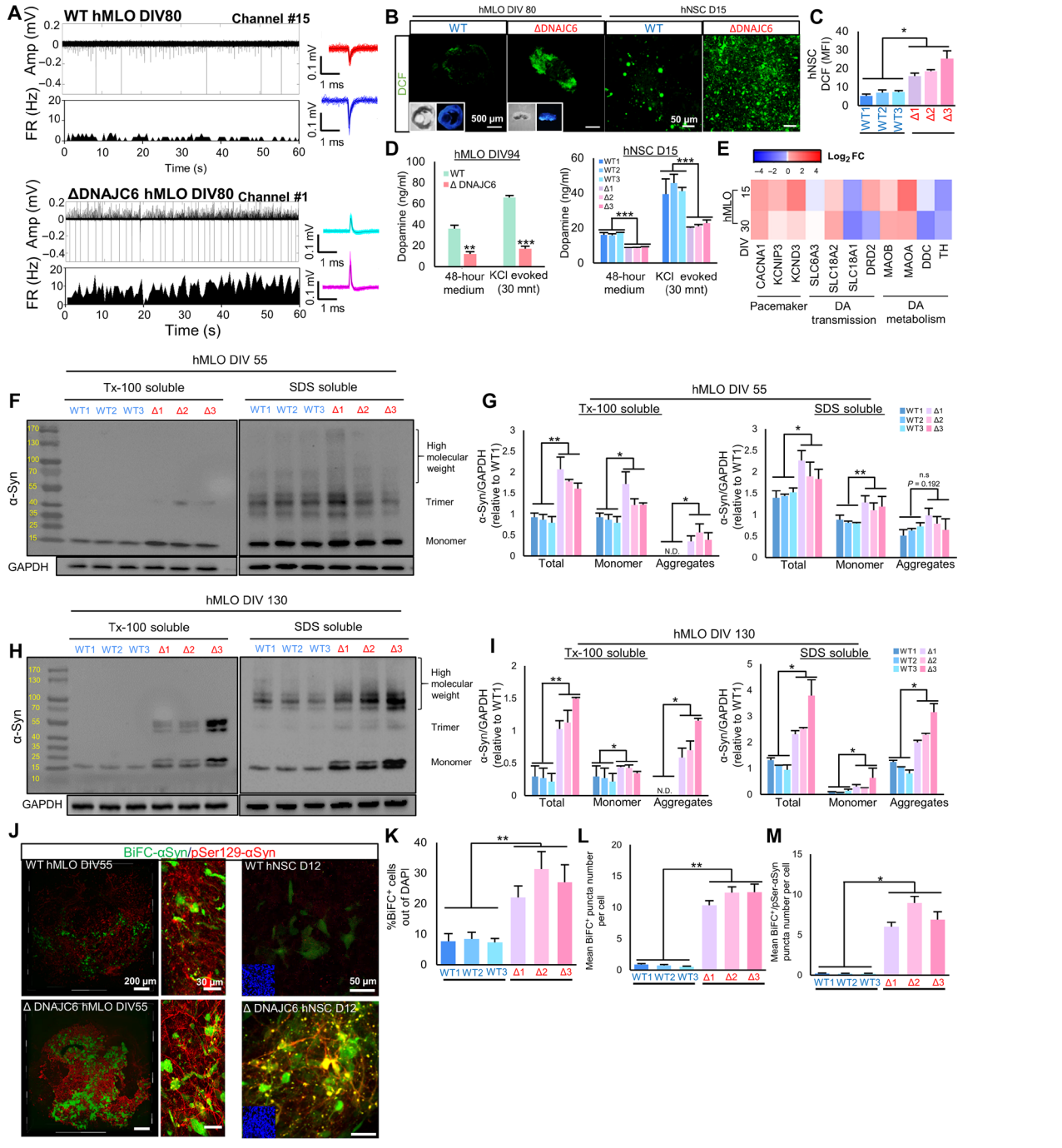

Fig. 4. Disease pathology in mutant *DNAJC6*. (**A**) Transient plots from multielectrode array with representative sorted neural signals and the firing rate of the neural signals over time recorded from WT and Δ*DNAJC6* hMLO organoids using a 16-electrode silicon neural probe. (**B** and **C**) Measurement of intracellular reactive oxygen species (ROS) in hMLO (scale bars, 500 μm) and differentiated NSC cultures (scale bars, 50 μm) through dihydrodichlorofluorescein diacetate (DCF) DA staining (B); ROS level is presented as mean fluorescence intensity value (C). $n = 3$ independent experiments. (**D**) Quantification of DA release in hMLO DIV94 and differentiated NSC D15. $n = 3$ independent experiments. mnt, minutes. (**E**) Heatmap for the expressions of DA metabolism, DA transmission, and pacemaker-related genes in the RNA-seq data. Expression value is shown as $\log_2$ fold change of Δ*DNAJC6* versus WT hMLO DIV15 and DIV30, respectively. (**F** to **I**) WB analyses to determine endogenous α-syn protein levels from Triton X-100 (Tx-100)–soluble and –insoluble fractions of WT and Δ*DNAJC6* hMLO at DIV55 and DIV130 (F and H). Intensities of the bands in (F) and (H) were quantified using ImageJ software, and the values were normalized to GAPDH (G and I). $n = 3$ independent experiments. (**J** to **M**) Intracellular detection of α-synuclein aggregation using bimolecular fluorescence complementation (BiFC) on hMLO DIV55 and hNSC D12 (I). Analysis on hMLO DIV55 was conducted using CLARITY imaging and further confirmation by sectioned organoid (thickness, 30 μm) from the same batch and analyzing it using confocal (J). α-Syn aggregation shown in terms of the percentage of $BiFC^+$ cells, $n = 3$ independent experiments (K), number of $BiFC^+$ puncta per cell (L), and number of $BiFC^+$/pSer129-αSyn^+ puncta per cell (M), $n = 30$ cells analyzed in each group. Scale bars, CLARITY, 200 μm; 30 μm for high-magnification image; hNSC, 50 μm. N.D., not detected. Data are presented as means ± SEM. Significance at $^*P < 0.05$; $^{**}P < 0.01$; $^{***}P < 0.001$, Student's *t* test.

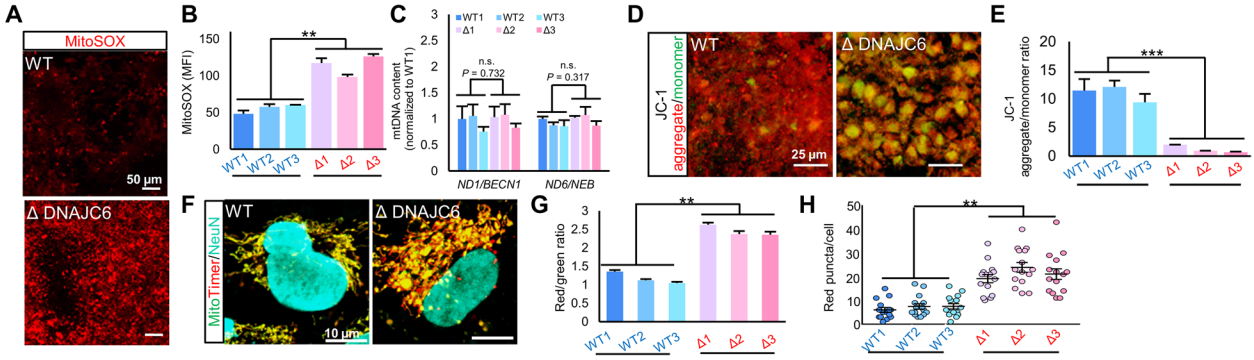

Fig. 5. Mitochondrial dysfunction in *DNAJC6* mutants. (**A** and **B**) Mitochondrial ROS in differentiated NSC culture were detected using MitoSOX Red probes (A). Fluorescence intensity was measured using ImageJ in 15 different areas from three independent experiments (B). ROS levels are presented as mean fluorescence intensity. Scale bars, 50 μm. (**C**) qRT-PCR analysis of mitochondrial DNA ratio in WT and mutant neurons, ($n = 3$). (**D** and **E**) Mitochondrial membrane potential analysis with JC-1 in differentiated NSC culture (D). A decrease in the red fluorescence (JC-1 aggregate)/green fluorescence (JC-1 monomer) ratio indicates depolarization/disruption of the mitochondrial membrane potential (E). Scale bars, 25 μm. (**F** to **H**) Representative images of *MitoTimer* reporter gene expression in differentiated NSC cultures (F). Red fluorescence represents oxidized Ds-Red mutant (DsRed1-E5) caused by oxidative stress. Mitochondria damage was measured as the red:green ratio (G) and number of pure red puncta per cell. $n = 15$ cells from each group (H). Scale bar, 10 μm. Data are presented as means ± SEM, $n = 3$ independent experiments. Significance at $^{**}P < 0.01$; $^{***}P < 0.001$, Student's *t* test.

To further validate mitochondrial damage in the mutant cultures, we used a stable expression of MitoTimer, encoding Timer protein [DsRed mutant (DsRed1-E5)] fused with the mitochondrial signal sequence from the cytochrome *c* oxidase subunit VIII (COX8). DsRed mutant emanates green fluorescence when newly synthesized but shifts the fluorescent spectrum irreversibly to red when oxidized; therefore, it can also be used to monitor mitochondria damage due to oxidative stress (*45*). We found that mutant neurons showed higher intensity of red fluorescent and more pure red puncta, indicating damaged mitochondria (Fig. 5, F to H). Mitochondrial contents, estimated by mitochondrial DNA copy number, were indistinguishable between WT and mutant cells (Fig. 5C), indicating that mitochondrial load did not seem to affect the observed findings for mitochondrial damage.

Impairment of autophagic clearance of α-syn is one of the main causes of α-syn accumulation in PD (*46*, *47*). We found an increase of autophagosome components p62 and LC3II protein levels in mutant neurons (Fig. 6, A and B, left). Consistently, as assessed by immunostaining, mutant neurons showed higher number of $p62^+$ puncta, along with the increase of $LC3II^+/p62^+$ colocalization (Fig. 6, C to E), collectively indicating that autophagosomes were accumulated either by increased initial autophagosome formation or by blockage of autophagic flux. The increase of $p62^+$ puncta was not accompanied by an increase of its mRNA expression (fig. S9A). In addition, upon bafilomycin A1 treatment, which blocks fusion between autophagosome and lysosome, the protein levels of LC3B-II and p62 significantly increased in WT neurons, but not in mutant neurons (Fig. 6, A and B, right), suggesting that the increase of $LC3^+/p62^+$ autophagosomes in the mutant neurons is likely due to an inefficient autophagy flux. We further examined the autophagic flux using the mCherry-GFP-LC3B tandem fluorescent probe, which emanates both mCherry and green fluorescent protein (GFP) signals in the stage of autophagosome, but only mCherry fluorescence in autolysosomes owing to its acidic pH of autolysosome. Compared to WTs, the mutant neurons transduced with the probe vector showed increased $mCherry^+/GFP^+$ autophagosomes at the expense of $mCherry^+$ autolysosomes (Fig. 6, F to H). Reduced autolysosomes in the mutant neurons were further confirmed by the decrease in $LAMP1^+/LC3^+$ puncta (Fig. 6, I and J), collectively indicating that autophagy flux was blocked at the late stage. Total $LAMP1^+$ (Fig. 6K) and $LysoTracker^+$ puncta (fig. S9, B and C) were also significantly lower in the mutant cells. The lysosomal markers [lysosomal-associated membrane protein 1 (LAMP1)] are also expressed in the late endosomes, which can be discriminated from lysosome by the expression of mannose-6-phosphate receptor (M6PR) (*48*). LAMP1 and M6PR coimmunostaining further confirmed the decrease in $LAMP^+/M6PR^-$ lysosome puncta (fig. S9, D and E), indicating that the decrease in $LAMP1^+/LC3^+$ colocalization was likely an indication of the lower lysosomal number. In contrast, numerous LC3 puncta were colocalized with LAMP1 in mutant neuron (Fig. 6, I and J), indicating that the fusion between the autophagosome and lysosome was normal in mutant neuron.

Furthermore, lysosomes ($LAMP1^+/M6PR^-$) were enlarged in *DNAJC6* mutant neurons (fig. S9, D and G), indicating impairment of degradation processes in lysosomes in the mutant cells. To assess lysosomal degradation capacity, we measured two representative enzyme activities [glucocerebrosidase 1 (GBA1) and cathepsin D], decreases of which are closely linked to PD (*49*, *50*). GBA1 expression (Fig. 6P and fig. S9I) and total (cytosolic and lysosomal) GBA1 enzyme activity were indistinguishable between the mutants and WTs (fig. S9H). However, along with a decrease in colocalization of GBA and lysosomes ($LAMP1^+$) (Fig. 6, N and O), lysosomal GBA activity was significantly reduced in the mutant cells (Fig. 6L). Furthermore, the activity of cathepsin D, a downstream target of GBA that is directly involved in lysosomal degradation process of α-syn (*51*), was also significantly decreased (Fig. 6M). Lysosomal proteins are processed by vesicular trafficking via endoplasmic reticulum (ER) and Golgi apparatus. Previous findings showed that overexpression of α-syn in mouse neurons can inhibit intracellular trafficking of GBA, leading to the increased retention of GBA in the ER and the decreased GBA in lysosomes (*52*, *53*). In agreement with these reports, GBA immunoreactivity was more abundant in the $calnexin^+$ ER compartments of the mutant neurons (Fig. 6, Q and R). Furthermore, the $LAMP1^+/M6PR^+$ late endosomes, involved in Golgi-to-lysosome vesicular transport, were also significantly reduced in the mutant neuronal cells (fig. S9, D and F). These findings collectively

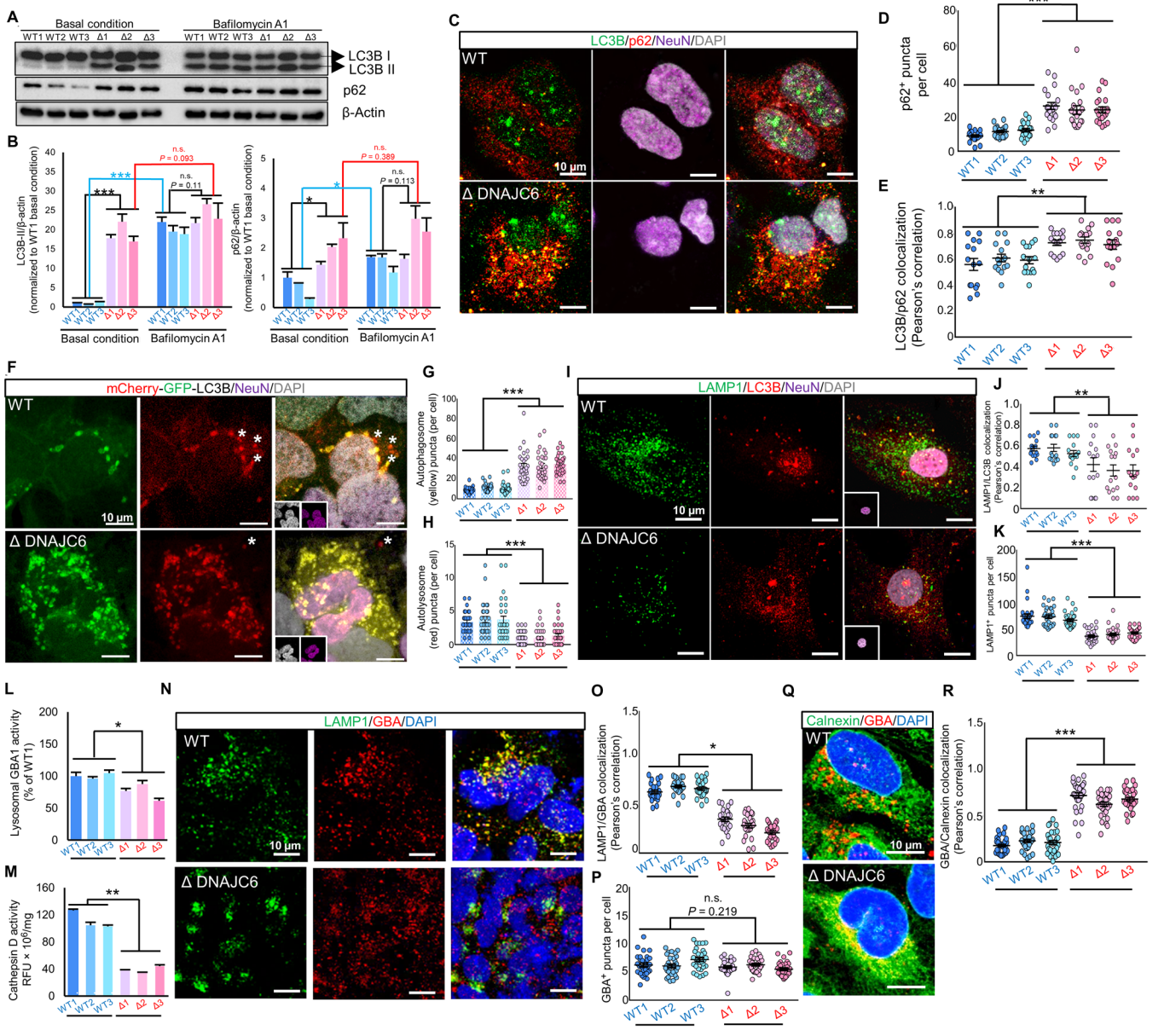

Fig. 6. Autolysosomal dysfunctions in *DNAJC6* mutant neuron. (**A** and **B**) WB analysis of the autophagosome components LC3BII and p62 in the presence or absence of bafilomycin A1. (B) represents the protein levels of LC3BII and p62 (normalized to β-actin) relative to the WT1 value at basal condition. $n = 3$ independent experiments. (**C** to **E**). Representative image of LC3B/p62 staining in differentiated neuron cultures (C). Scale bars, 10 μm for all images. Quantification of $p62^+$ puncta number per cell (D) and colocalization of $p62^+$ and $LC3^+$ puncta per cell (E). $n = 12$ cells (D) and $n = 15$ cells (E) from each group. (**F** to **H**) Representative image of differentiated neuron expressing mCherry-GFP-LC3B (F). Insets, $DAPI^+$ (gray) and $NeuN^+$ (purple) images in the same microscopic fields. Quantification of autophagosomes (yellow puncta) and autolysosomes (red puncta) number per cell (G and H). $n = 30$ cells. Asterisk (*) symbols indicate autolysosomes. (**I** to **K**) Representative image of LAMP1/LC3B staining in differentiated neurons (I). Inset, $DAPI^+/NeuN^+$ image. Colocalized $LAMP1^+$ with $LC3^+$ puncta per cell (J). $LAMP1^+$ puncta per cell (K). $n = 15$ (J) and $n = 30$ (K) cells. (**L** and **M**) Lysosomal glucocerebrosidase 1 (GBA1) (L) and cathepsin (M) activities. $n = 3$ biological replicates. (**N** to **P**) Representative $LAMP1^+/GBA^+$ images in differentiated neuron (N). The numbers of colocalized $LAMP1^+/GBA^+$ puncta (O) and GBA^+ puncta (P) per cell were quantified. $n = 24$ (O) and $n = 20$ (P) cells. (**Q** and **R**) Representative $calnexin^+/GBA^+$ images (Q). The numbers of colocalized $calnexin^+/GBA^+$ puncta per cell (R). $n = 30$ cells. Data are presented as means ± SEM. Significance at $^*P < 0.05$; $^{**}P < 0.01$; $^{***}P < 0.001$, Student's *t* test.

suggest that the loss of *DNAJC6* function causes an impairment in vesicular transport process of lysosomal proteins and ultimately a decrease in lysosomal enzyme activities. Consistent with the impaired autolysosomal degradation processes, α-syn protein was more stable in *DNAJC6* mutant neuronal cells than in WT neurons (fig. S9, J and K).

DNAJC6 knocked down in the VM-patterned NSCs replicates PD pathologic findings

When *DNAJC6* gene knockdown (KD) was conducted in a WT VM-NSC culture using CRISPR-interference (CRISPRi) (*54*), we also observed the reduced midbrain factor expression in differentiated DA neurons (fig. S10, A to M). DA neurons differentiated from

KD NSCs also have fragmented neurites (fig. S10N) and increased α-syn aggregation (fig. S10, O to Q). Considering that the VM pattern of the NSC culture was already determined, these findings indicate that, in addition to DNAJC6 expression during the early developmental period for VM pattering, its maintenance afterward is critical to prevent mDA neurons against loss of critical midbrain factor expressions and degeneration that can lead to PD phenotypes.

DNAJC6 may have a role in autolysosomal degradation of α-syn in an LMX1A-independent manner

Forced expression of *DNAJC6* in mutant hESCs rescued the defects in organoid development into hMLOs with recovered WNT-LMX1A signals (fig. S11, A to C), and the rescued hMLOs therefore yielded mDA neurons that expressed midbrain-specific factors comparable to those of the WTs with improved mitochondrial function in differentiated neuron cultures (fig. S11, D and E). Exogenous *DNAJC6* expression in mutant NSC cultures could also almost completely rescue all PD phenotypes in differentiated mDA neuronal cells (Fig. 7, A to F). Given that LMX1A is a critical factor mediating the observed DNAJC6 roles, cell viability and mitochondrial function were improved by forced expression of *LMX1A* in mutant NSC cultures (Fig. 7C). However, lysosomal defects, as estimated by lysosomal number, size, and GBA protein localization, were not significantly rescued by forced *LMX1A* expression (Fig. 7, D and E). In addition, accumulation of pathologic α-syn (p129-α-syn$^+$, ProteoStat$^+$ puncta), which is largely affected by lysosomal (GBA) functions, was insignificantly rescued by *LMX1A* expression (Fig. 7F). Consistently, *LMX1A* KD using lenti-shLMX1A in WT-NSC cultures resulted in a significant decrease in DA neuronal yield, survival, midbrain-specific factor expression, and mitochondrial health (fig. S12, A to Q), without alteration in the lysosomal number, GBA localization in lysosome, and autophagy flux (fig. S12, R to X). These findings collectively indicate that autolysosomal defects in *DNAJC6*-mutant neurons are not mediated through the down-regulation of *LMX1A*. However, we noticed that α-syn aggregation, estimated by the number of BiFC$^+$/p129-α-syn$^+$ puncta, was significantly increased by *LMX1A* KD in WT neuronal cultures (fig. S12AA), which is likely due to mitochondrial and oxidative damage caused by *LMX1A* KD in the neuronal cells (fig. S12, N to Q).

DNAJC6 mutation causes general neurogenesis impairment

A remaining question is whether loss of DNAJC6 functions is specific to the mDA neuron system or causes a generalized neuronal deficit. In addition to reduced DA neuronal yield (fig. S14, A to D), the TUJ1$^+$ and MAP2$^+$ generic neuronal population were also lower in *DNAJC6* mutant hMLOs (fig. S14, E to G) and differentiated VM-NSC cultures (fig. S14, H to J). Furthermore, when the mutant hESCs were induced to differentiate into organoids that resembled cortical brain, neuronal yield in the cortical organoids carrying the *DNAJC6* mutation was also decreased (fig. S15, B to D) with lower expression of cortical neuron-specific markers compared to WT cortical organoids (fig. S15E). The expression of the forebrain-specific neural precursor markers (*PAX6*, *TBR2*, and *HOPX*) was rather greater in the mutant cortical organoids (fig. S15E), indicating impaired cortical neurogenesis due to DNAJC6 loss. The observed extra-midbrain defect is consistent with the mental retardation and seizures frequently detected in patients with *DNAJC6*-PD (*4*). Despite this generalized deficit, impaired neuron development may have a more profound impact on the midbrain DA neuron system, and ultimately prominent PD symptoms in patients who carry *DNAJC6* mutations, due to the unique development of mDA neurons, in which developmental factors such as LMX1A, EN1, and NURR1 continue to be expressed and have roles in adult mDA neurons that prevent their degeneration. This is also due to the vulnerability of mDA neurons owing to high intracellular ROS, intrinsic firing frequency, and energy demand [reviewed in (*55*)].

In summary, using the *DNAJC6*-PD human disease model, we identified that loss of DNAJC6 during mDA neuron development causes loss of *LMX1A* expression through impaired WNT signaling (Fig. 7G, left). The impaired expression of LMX1A and NURR1 (a downstream target of *LMX1A*) continues and induces mitochondrial defects and oxidative stress in differentiated mDA neuronal cells (Fig. 7G, right). On the other hand, loss of DNAJC6 directly causes autolysosomal defects in mDA neurons in an LMX1A-independent manner. The LMX1A-dependent and -independent cellular dysfunctions together additively induce PD manifestations such as pathologic α-syn aggregation and mDA neuron degeneration.

DISCUSSION

With absence of animal model replicating PD phenotypes and with limitation in obtaining samples from the patients, mechanistic understanding for the juvenile and/or early-onset PD with *DNAJC6* mutations has remained unexplored. In this study, we generated and analyzed human midbrain organoids and mDA neurons derived from the isogenic hESCs carrying *DNAJC6* mutations. PD-like phenotypes, such as mDA neuronal degeneration, stressful pacemaking, and synucleinopathy with intracellular oxidative stress and autolysosomal and mitochondrial defects, were produced in the hMLO and mDA neuron cultures derived from the mutant hESCs, indicating that the experimental system we generated is an effective human disease model for studying *DNAJC6*-PD. Analyses of our model revealed that the loss of DNAJC6 functions in early development impaired the VM patterning and, in turn, caused defects in establishing a battery of the midbrain-specific marker expressions in adult mDA neurons. The latter would be critical for survival, phenotype maintenance, and functions of the mDA neuronal cells (*18*–*20*). Collectively, our study suggests that early developmental loss of DNAJC6 results in the mDA neurons vulnerable to neurodegeneration, along with multiple PD phenotypes.

We have identified LMX1A as the central factor mediating the developmental role of DNAJC6, a defect associated with PD phenotypes in mDA neurons. Supporting this, forced expression of *LMX1A* in *DNAJC6* mutant cultures has rescued the defects in the midbrain factor expressions and mitochondrial function. However, lysosomal defects and α-synucleinopathy were not significantly rescued in the mutant mDA neuron cultures by the *LMX1A* expression. Considering the physiological functions of DNAJC6 in controlling CME (*2*), these findings suggest that DNAJC6 is likely to directly regulate the vesicular trafficking of lysosomal proteins, hence the lysosomal clearance of α-syn in neuronal cells without the involvement of LMX1A. Therefore, we propose that the loss of DNAJC6 can lead to the PD pathogenesis process in two ways: one is through the LMX1A-dependent transcription of mDA-specific genes and the other is through the molecular chaperone function of DNAJC6 regulating vesicle trafficking.

In this study, we showed that loss of DNAJC6 function causes autophagy defects and that α-syn is accumulated due to impaired autophagy-lysosomal degradation in the *DNAJC6* mutant neuronal

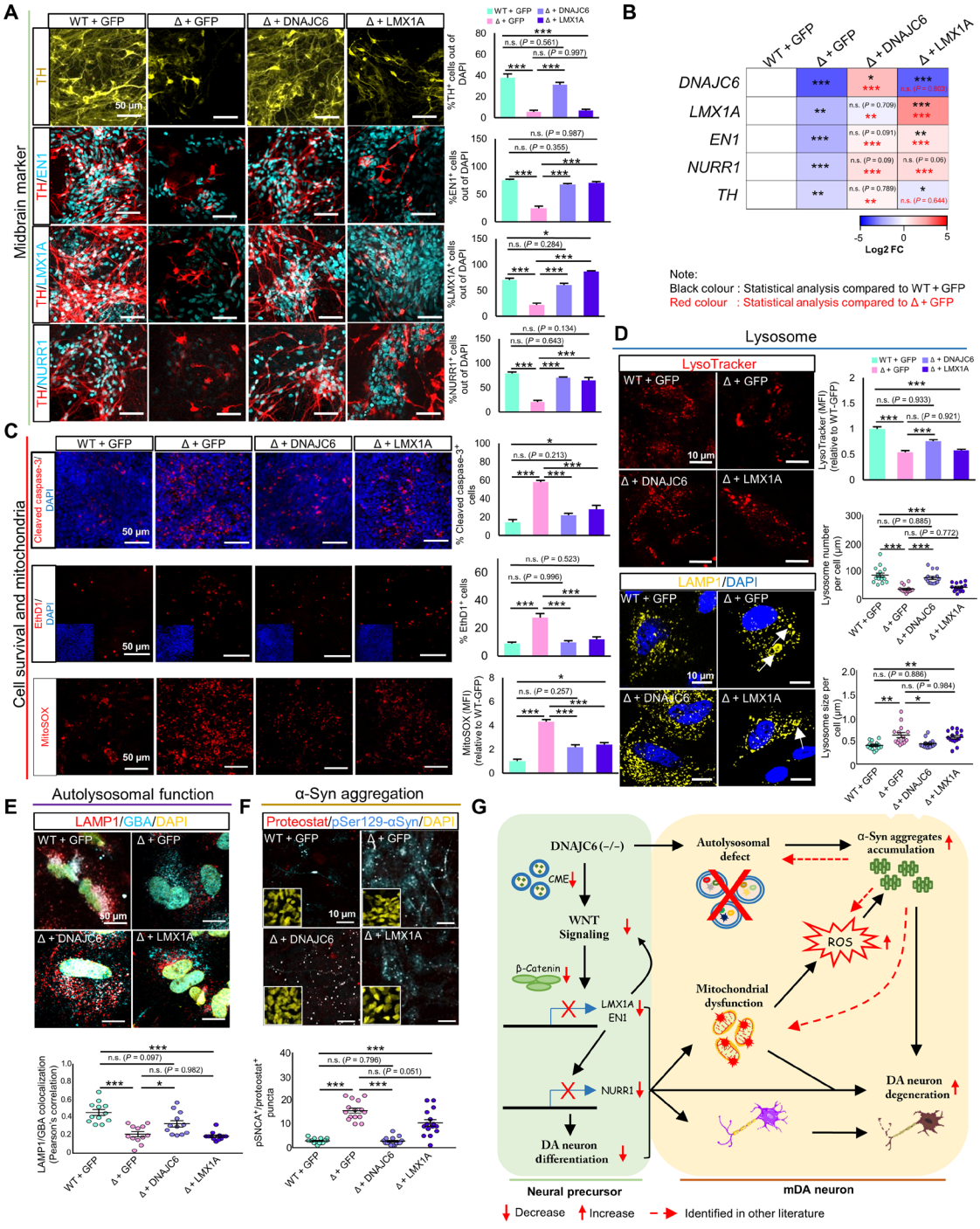

Fig. 7. DNAJC6 does not require LMX1A in preventing lysosomal dysfunction. DNAJC6 mutant (△3) NSCs were transduced with the lentiviruses expressing LMX1A, DNAJC6, or GFP (control) and then differentiated into mDA neurons. (**A** and **B**) Expression of midbrain-specific factor was determined in the differentiated mDA neuronal cultures using immunocytochemical (A) and qPCR (B) analyses. Scale bars, 50 μm. $n = 3$ independent experiments. (**C**) Cell viability assessed by the number of cleaved caspase-3$^+$ and EthD1$^+$ cells (first and second rows) and mitochondrial ROS estimated by MitoSox (third row). Scale bars, 50 μm. $n = 3$ independent experiments. (**D**) LMX1A and DNAJC6 rescuing effects on amount and size of lysosome. Confocal microscopy for LysoTracker Red DND99 in differentiated neurons. Scale bars, 10 μm. Averages of mean LysoTracker fluorescence intensities per cell are quantified in the graph at the first row. $n = 15$ cells from each group. Visualization of lysosome by LAMP1 staining in differentiated neurons. Scale bars, 10 μm. Quantification of lysosome number per cell (second graph) and lysosome size per cell (third graph), $n = 15$ cells from each group. Each dot represents the average value of lysosome size per cell. The white arrow indicates an enlarged lysosome. (**E**) Representative image of LAMP1/GBA staining in differentiated neurons. Scale bars, 50 μm. Quantification of colocalized LAMP1$^+$ and GBA$^+$ puncta per cell. $n = 15$ cells from each group. (**F**) LMX1A and DNAJC6 rescuing effects on α-syn aggregation in differentiated neuron. The α-syn aggregation was quantified by the number of pSer129-αSyn$^+$/ProteoStat$^+$ puncta per cell. Scale bars, 10 μm. $n = 15$ cells from each group. (**G**) Schematic summary for PD pathogenic signaling pathways caused by loss of DNAJC6. Data are presented as means ± SEM. Significance at $^*P < 0.05$; $^{**}P < 0.01$; $^{***}P < 0.001$, one-way ANOVA with Bonferroni post hoc analysis.

cells. Specifically, autolysosome formation caused by reduced lysosome number and vesicular transport of lysosomal enzymes were defected in the mutant cells. It has been reported that functional lysosomes are regenerated by an autophagic lysosome reformation process, the terminal step of autophagy, which involves the clathrin function necessary for proto-lysosome budding from reformation tubules (*56*, *57*). Similarly, Golgi-to-lysosome protein transport is also mediated by clathrin-mediated vesicular trafficking. In *DNAJC6* mutant cells, the number of free clathrin is expected to decrease owing to the defect in the clathrin uncoating process. This might explain why the autophagy-lysosomal process is impaired in *DNAJC6* mutant neurons in our study (Fig. 6).

The midbrain factors, LMX1A, EN1, and NURR1, promote mitochondrial biogenesis and functions (*21*, *23*, *24*), and therefore, the loss of the midbrain factors would cause mitochondrial damage, which was validated in our experiments with the *DNAJC6* mutant neuronal cultures. Because of the impaired antioxidant and Ca^{2+} buffering capacities in damaged mitochondria, intracellular ROS and Ca^{2+} levels are increased in *DNAJC6* mutant neurons. Perhaps, the increased α-syn aggregation in these cells might be partly due to the high ROS and Ca^{2+} intracellular environments [reviewed in (*44*)]. On the opposite side, toxic α-syn oligomers and aggregates can cause mitochondrial damage/dysfunctions and oxidative stresses [reviewed in (*58*)], which would create a positive-feedback loop between mitochondrial/oxidative stresses and α-synucleinopathy. In addition, the impairment of autolysosomal degradation in *DNAJC6* mutant cells would further contribute to the accumulation of intracellular toxic α-syn, which would in turn cause another positive-feedback loop between lysosomal dysfunction and toxic α-syn accumulation. Increased ROS (Fig. 4, B and C), reduced DA release (Fig. 4D), and aggregated α-syn (Fig. 4, F to I) elevated the intrinsic firing frequency in the mutant DA neurons (Fig. 4A) (*40*–*42*). The overworked intrinsic pacemaking would make the mutant neurons more vulnerable to toxic insults (*59*, *60*).

The early developmental contribution of the *DNAJC6* mutations was not anticipated based on the previous studies using animal models. *DNAJC6* has been known as a neuronal gene, expression of which commences at the later stages in neural tissues in rodent models (*3*, *6*). Consistently, we also observed that mouse *Dnajc6* expression was undetectable in mouse ESC (mESC) stage but became detectable from VM tissue at embryonic day (E) 12 (fig. S13A). In contrast, mRNA and protein expressions of human DNAJC6 were readily detected from the hESC stage, equivalent for blastocyst of human embryo (Fig. 1, C to E, and fig. S13B). To confirm the human-specific expression of *DNAJC6* in the early developmental stage, we used another hESC (HuES6) and induced pluripotent stem cell [iPSC (Epi-iPSC)] line. We found that all the hESCs and iPSCs used in this study have the same levels of *DNAJC6* and showed similar expression pattern (fig. S13, B and C), suggesting the species-dependent differences in developmental pattern of *DNAJC6* expression. Another human-specific difference from mouse was that there was no compensatory up-regulation of cyclin G associated kinase (*GAK* or *Auxilin-2*), a homologous protein of DNAJC6, in the human midbrain organoids and cells carrying the deleterious *DNAJC6* mutations. A previous study has shown that GAK was up-regulated and compensated for the absence of DNAJC6 in the knockout mouse brains (*6*). In agreement with this report, we also found that *Auxilin-2* (*Gak*) mRNA and protein levels were increased when we knocked down *Dnajc6* on WT mouse NSC using CRISPRi, but not in human NSCs (fig. S13, D to I). Similarly, no redundant increase of *GAK* was shown in the human *DNAJC6* loss-of-function mutant organoids (hMLOs, DIV30; fig. S13, J to L). In addition, we were not able to find any decrease in midbrain-specific marker expression and DA neuron yield in the mouse culture (fig. S13, M and N). These data suggest that the redundancy of *Dnajc6* and *Gak* is attributed to the lack of overt PD phenotypes in the knockout mice. Given these overt species differences, we suggest that human brain diseases associated with DNAJC6 should be studied in human disease models.

Developmental aspects have been suggested as a contributing factor for PD pathogenesis (*7*). However, compelling evidence has been missing to support this idea. Our current study using a human disease model for PD with *DNAJC6* mutation provides such evidence that developmental defects can be the critical contributing factors to cause the juvenile-onset PD. On the basis of our study, we propose that developmental aspect would be one of the parameters to be considered in diagnosis and treatment when evaluating a patient for early or juvenile-onset PD.

MATERIALS AND METHODS

Human ESC cultures

Human ESCs and human iPSCs used were maintained on Matrigel (Corning Life Sciences, USA) in mTeSR1 medium (STEMCELL Technologies) supplemented with doxycycline (1 μg/ml) with change of medium daily. All of the information on hESCs and hiPSCs used in this study are listed in table S1.

Mouse ESC cultures

R1 mESCs were cultured without irradiated murine embryonic fibroblasts and grown on gelatinized tissue culture plates in Dulbecco's Modified Eagle medium (DMEM) with 20% heat-inactivated fetal bovine serum (FBS), nonessential amino acids (0.1 mM), L-glutamine (2 mM), β-mercaptoethanol (0.1 mM), and recombinant mouse leukemia inhibitory factor (LIF) (1000 IU/ml; PeproTech) in a humidified 37°C incubator with 5% CO_2.

Mouse VM-NSC cultures

Mouse VM-NSCs were cultured from mouse embryo VMs (ICR) at E10 on 6-cm dishes or 24-well plates precoated with poly-L-ornithine (15 μg/ml) (Sigma-Aldrich)/fibronectin (1 μg/ml) (Sigma-Aldrich, St. Louis, MO) in serum-free N2 medium supplemented with mitogen basic fibroblast growth factor (bFGF, 20 ng/ml, and EGF, 20 ng/ml, R&D Systems, Minneapolis, MN). The proliferating VM-NSCs cultured in 6-cm dishes were passaged at every fourth day in mitogen-supplemented medium. The expanded NSCs at the last day of each passage were induced to differentiate by withdrawing the mitogen from the media (for 7 to 9 days).

Generation of isogenic hESCs harboring the DNAJC6 mutation

Plasmids carrying Cas9 (pRGEN-CMV-Cas9-RFP-Puro, 3 μg) and sgRNA targeting the *DNAJC6* gene region encompassing the intron 6–exon 7 junction (ACCTTCTGTTTCAGATACCT, pRGEN-U6-SGhDNAJC6, 3 μg) were introduced to hESCs (1×10^6 cells/100 μl) using a NEPA21 electroporator (NEPAGENE) following the manufacturer's instruction. Transfected hESC colonies were identified by red fluorescence (RFP expression) and selected using puromycin treatment (50 mg/ml). The puromycin-selected colonies were picked, seeded into 96-well plates (1 cell per well), and expanded. The targeted region of *DNAJC6* gene was amplified using touchdown PCR and

subjected to T7E1 assay (NEB) to detect the gene-edited clones. The PCR-amplified fragments were cloned in a TA-cloning vector and subjected to Sanger sequencing to confirm the edited nucleotide sequence. To characterize hESC chromosomal integrity after editing using CRISPR-Cas9, hESCs were karyotyped using the standard protocol for high-resolution G-banding.

Cell growth assays

The cell growth profile during hESC expansion with several cell passages was generated by counting the number of viable cells at the end of each passage. Cell expansion of each hESC passage was further estimated by the population doubling level, which was determined by $\log(N/N0)/\log_2$ [where N is the number of cells at the end of each passage; $N0$ is the number of cells plated initially (1×10^5 cells/cm^2)].

Plasmid construction for lentiviral vector expressing DNAJC6, SNCA, LMX1A, BiFC-SNCA, and mCherry-GFP-LC3B tandem fluorescent probe

Lentiviral vectors expressing human DNAJC6 were obtained by modifying pLX304-DNAJC6-WT-V5 plasmids obtained from Harvard (#HsCD00414238), and a DNAJC6 insert sequence was amplified by PCR with the addition of Eco RI and Not I restriction sites at 5′ and 3′. The PCR products were inserted to the MCS of the pCDH-EF1-MCS-T2A-copGFP vector (System Biosciences, #CD526A1) to generate pCDH-EF1-DNAJC6-T2A-copGFP.

To generate lentiviral vectors expressing WT-SNCA (synuclein alpha), full cDNA sequences of human SNCA were amplified by PCR with the addition of Bstb I and Asc I restriction sites at 5′ and 3′. The PCR products were inserted to the multi-cloning site (MCS) of the pCDH-EF1-MCS-T2A-copGFP vector (System Biosciences, #CD526A1) to generate pCDH-EF1-SNCA-T2A-copGFP.

To generate lentiviral vectors expressing WT-LMX1A, full cDNA sequences of human LMX1A were amplified by PCR with the addition of Nhe I and Not I restriction sites at 5′ and 3′. The PCR products were inserted to the MCS of the pCDH-EF1-MCS-T2A-copGFP vector (System Biosciences, #CD526A1) to generate pCDH-EF1-LMX1A-T2A-copGFP.

To generate lentiviral vectors expressing BiFC-SNCA, plasmid vectors expressing human SNCA-VC and SNCA-VN were obtained by modifying SNCA-VC and VN-SNCA plasmids obtained from Addgene (#89471; #89470). SNCA-VC and VN-SNCA insert sequences were amplified by PCR with the addition of Not I and Sal I restriction sites at 5′ and 3′. The PCR products were inserted to the MCS of the pCDH-EF1-MCS-T2A-copGFP vector (System Biosciences, #CD526A1) while also removing copGFP to generate pCDH-EF1-SNCA-VC and pCDH-EF1-VN-SNCA.

To generate lentiviral vectors expressing mCherry-GFP-LC3B, plasmid vectors expressing human LC3B in tandem with mCherry and GFP were obtained by modifying FUW-mCherry-GFP-LC3 plasmids obtained from Addgene (#110060), and an mCherry-GFP-LC3B insert sequence was amplified by PCR with the addition of Bam HI and Sal I restriction sites at 5′ and 3′. The PCR products were inserted to the MCS of the pCDH-EF1-MCS-T2A-copGFP vector (System Biosciences, #CD526A1) while also removing copGFP to generate pCDH-EF1-mCherry-GFP-LC3B.

Lentivirus production and transduction

Vesicular stomatitis virus G (VSVG) protein–coated lentiviruses were generated in human embryonic kidney (HEK) 293 cells. Briefly, HEK 293 cells were transfected using Lipofectamine 2000 (Invitrogen), with a mixture of lentiviral construct and second-generation packaging plasmids. The culture medium was changed after 24 hours and collected 96 hours after transfection. Virus-containing medium was filtered through a 0.45-μm filter and concentrated using polyethylene glycol precipitation. Virus titer was determined using the QuickTiter HIV Lentivirus Quantitation Kit [HIVp24 enzyme-linked immunosorbent assay (ELISA), Cell Biolabs]. For viral transduction, NSCs were incubated with viral supernatant [10^6 TU (transducing unit)/ml] containing polybrene (6 μg/ml) overnight, followed by a medium change.

Generation of hMLOs

hMLOs were generated as previously described (*38*) with small/slight modifications. The protocol is schematized in fig. S3A. Briefly, hESCs dissociated with Accutase (STEMCELL Technologies) were plated at 10,000 cells per well in 96-well plates (low-attachment, round-bottom, Corning) in a neuronal induction medium [N2 2×:Neurobasal medium (1:1) containing 1:50 B27 without vitamin A (Invitrogen), 1% GlutaMAX (Invitrogen), 1% minimum essential media–nonessential amino acid (Invitrogen), and 0.1% β-mercaptoethanol (Invitrogen), 10 μM SB431542 (Stemgent), Noggin (200 ng/ml) (Prospec), 0.8 μM CHIR99021 (Reagents Direct), 10 μM ROCK inhibitor Y27632 (Calbiochem), and doxycycline (1 μg/ml)]. On day 4, 2 μM purmorphamine, SHH-C25II (100 ng/ml) (R&D Systems), and FGF8 (100 ng/ml) (R&D Systems) were added for VM patterning. On day 8, hMLOs were embedded with Matrigel and cultured with shaking on an orbital shaker (West Tune) in a tissue-growth induction medium (Neurobasal) containing 1:100 N2 supplement (Invitrogen), 1:50 B27 without vitamin A (Invitrogen), 1% GlutaMAX (Invitrogen), 1% minimum essential media–nonessential amino acid (Invitrogen), 0.1% β-mercaptoethanol (Invitrogen), insulin (2.5 μg/ml) (Sigma-Aldrich), laminin (200 ng/ml) (Sigma-Aldrich), 2 μM purmorphamine, SHH-C25II (100 ng/ml) (R&D Systems), and FGF8 (100 ng/ml) (R&D Systems). One day later, the hMLOs were transferred into ultralow-attachment six-well plates (Costar) in a terminal differentiation medium (Neurobasal) containing 1:100 N2 supplement (Invitrogen), 1:50 B27 without vitamin A (Invitrogen), 1% GlutaMAX (Invitrogen), 1% minimum essential media–nonessential amino acid (Invitrogen), 0.1% β-mercaptoethanol (Invitrogen), brain-derived neurotrophic factor (10 ng/ml) (BDNF) (PeproTech), glial cell–derived neurotrophic factor (10 ng/ml) (GDNF) (PeproTech), 100 μM ascorbic acid (Sigma-Aldrich), and 125 μM db-cyclic adenosine 3′,5′-monophosphate (cAMP) (Sigma-Aldrich). The medium was changed every 3 days.

Derivation of VM-type NSC cultures from hMLOs

The H9 hESC lines were cultured feeder-free on Matrigel (Corning) with mTeSR1 (STEMCELL Technologies). The hESCs were dissociated to single cells with Accutase (STEMCELL Technologies), and 10,000 cells were plated in each well of low-cell adhesion 96-well culture plates with round-bottom conical wells (Corning) to form uniform embryoid bodies (EBs) in a neural induction medium. The neural induction medium from day 1 was N2 2×:Neurobasal (1:1; Gibco) containing B27 without vitamin A (2%; Invitrogen Fisher Scientific), SB431542 (10 μM; Tocris), Noggin (200 ng/ml; PeproTech), and ascorbic acid (200 μM; Sigma-Aldrich). To enrich VM-type NSC populations in hMLOs, modifications were made as illustrated in fig. S3B. The concentrations of the reagents treated were identical to those of the hMLO protocol except the CHIR99021 concentration

was doubled from day 11. The hMLOs were chopped and dissociated with Accutase and plated on vitronectin-coated 6-cm plates (Corning, cells from 24 organoids per plate) in N2 expansion medium [N2 containing BDNF (10 ng/ml), GDNF (10 ng/ml), 200 μM ascorbic acid, FGF8b (100 ng/ml), bFGF (20 ng/ml), and doxycycline (1 μg/ml)] supplemented with 5 μM Y27632. The NSCs were expanded with cell passages at 5- to 7-day intervals. Y27632 was supplemented for 1 day only after cell passage. Terminal differentiation of NSCs was induced in N2 differentiation medium containing BDNF (10 ng/ml), GDNF (10 ng/ml), 200 μM ascorbic acid, and 500 μM db-cAMP.

Generation of human cortical organoids

Human cerebral-like organoids were generated as previously described (*61*) with modifications. The protocol is schematized in fig. S15A. Briefly, hESCs dissociated with Accutase (STEMCELL Technologies) were plated at 9000 cells per well in 96-well plates (low-attachment, round-bottom, Corning) to form single EB in medium containing DMEM/F12, 20% Knockout Serum Replacement (KSR), 3% FBS, 2 mM GlutaMAX, 1% nonessential amino acids, 50 nM β-mercaptoethanol, and bFGF (4 ng/ml). ROCK inhibitor Y27632 (50 μM) was included in the first 24 hours. EBs were maintained in 96-well plates for 6 days and then transferred to ultralow-attachment 24-well plates (Corning), in neural induction medium containing DMEM/F12, 1× N2 supplement, 1% nonessential amino acids, 2 mM GlutaMAX, and heparin (1 μg/ml) (STEMCELL Technologies). On days 10 to 12, human cortical organoids (hCOs) were embedded in 30 μl of Matrigel droplet and cultured in a neural maturation medium containing 50% DMEM/F12, 50% Neurobasal, 0.5× N2 supplement, 0.5× B27 supplement, 2 mM GlutaMAX, human insulin (2.5 ng/ml), 0.5% nonessential amino acids, and 25 nM β-mercaptoethanol in ultralow-attachment six-well plates (Costar). Embedded hCOs were cultured under stationary conditions for 4 days, followed by transfer to an orbital shaker (West Tune).

RNA extraction, reverse transcription, and qRT-PCR

Total RNAs were isolated using TRIzol Reagent (Invitrogen) and reverse-transcribed using the SuperScript III Kit (Invitrogen) to create cDNA. Transcript abundance was determined by qRT-PCR using SYBR Green PCR mix (Bio-Rad) and performed using the CFX Connect Real-Time System (Bio-Rad). The ΔΔCq method was used to normalize expression levels of each gene to that of glyceraldehyde-3-phosphate dehydrogenase. Primers used are listed in table S2.

DNAJC6 mRNA stability assay

The WT and DNAJC6 mutant hESCs were treated with the transcription inhibitor 5,6-dichloro-1β-D-ribofuranosylbenzimidazole (DRB, Sigma-Aldrich, 20 μg/ml) for 12 hours. Cells were collected during the DRB-treatment period and subjected to RT-PCR to determine time-dependent changes in DNAJC6 mRNA levels.

Preparation of cells extract and immunoblotting

Protein was extracted using a radioimmunoprecipitation assay buffer containing a protease inhibitor (Roche) and phosphatase inhibitor cocktails (Sigma-Aldrich). In the case of β-catenin immunoblot, cytosolic and nuclear fractions from hMLOs were prepared using EpiQuik kit (Epigentek). Protein concentrations were measured using the Bradford method (Bio-Rad). Protein samples were run on SDS–polyacrylamide gel electrophoresis (PAGE) gel (12% or 4 to 16% for α-syn aggregate detection), transferred to a nitrocellulose (or polyvinylidene fluoride) membrane, blocked, and then incubated with the primary antibodies listed in table S4. Signals were visualized with horseradish peroxidase–conjugated antibodies and captured with ChemiDoc (Bio-Rad, Hercules, CA).

Analyses for α-syn aggregate formation

Formation of α-syn aggregates were assessed in hMLOs (DIV55), hMLOs (DIV130), and differentiated NSC cultures transduced with lentiviruses expressing human α-syn (pCDH-EF1-SNCA-T2A-copGFP). Samples were prepared by lysing cells with 1% Triton X-100, and taking the supernatant after centrifugation (16,000*g*, Triton X-100 soluble), the pellet was dissolved in 1× Laemlli buffer (Bio-Rad) and sonicated briefly (SDS soluble). Protein concentration was measured using bicinchoninic acid (BCA) protein assay (Pierce). α-syn oligomers were detected with immunoblot (α-syn, BD) analyses on a gradient SDS-PAGE gel as described above. The levels of α-syn aggregation were also estimated using immunocytochemical analysis for p129-α-syn and BiFC assay. The hMLOs and/or hNSCs were cotransduced with lentiviruses expressing Venus1-α-syn (V1S; N-terminal of α-syn) and α-syn-Venus2 (SV2; C-terminal of α-syn), and BiFC-α-syn aggregates were visualized as Venus-positive signal.

Immunofluorescent and other live fluorescent staining

Cultured cells were fixed with 4% paraformaldehyde (PFA) for 20 min (except 15 min for p129-α-syn staining). For LAMP1, GBA, LC3, and p62 staining, cells were fixed with 4% PFA for 2 min followed by cold MeOH fixation for 10 min. hMLOs were fixed in 4% PFA for 30 to 60 min, incubated in 30% sucrose at 4°C until hMLOs sank down, and subsequently embedded in optimal cutting temperature compound (Sakura Finetek). Frozen hMLOs were cryosectioned at a thickness of 16 to 25 μm. Cultured cells and hMLO sections were blocked and incubated overnight at 4°C in a blocking solution containing the primary antibodies listed in table S4. Secondary antibodies tagged with Alexa 488, Alexa 647 (1:200; Invitrogen), and Cy3 (1:200; Jackson ImmunoResearch Laboratories) were applied. Stained samples were mounted in Vectashield medium containing 4′,6-diamidino-2-phenylindole (DAPI; Vector Laboratories, West Grove, PA). Images were taken using an epifluorescence (Leica) or a confocal microscope (Leica TCS SP5).

For live EthD1 and DCF-DA staining, hMLO (DIV > 80) was embedded in 5% low-gelling temperature agarose (Sigma-Aldrich, A9414) at 40°C in peel-a-way embedding mold. The agarose blocks were incubated on ice for 10 to 15 min and then sectioned using Vibratome in cold Hanks' balanced salt solution (HBSS) at a thickness of 300 μm. Sections were collected onto low-retention six-well plates and left to equilibrate overnight at 37°C in final differentiation medium supplemented with 10 μM ROCK inhibitor Y27632 (Calbiochem). Sections were then stained with EthD1 (Invitrogen) and/or DCF-DA (Calbiochem, 287810) as described in manufacturer protocols. For LysoTracker DND-99 (molecular probes) and MitoSox staining, cells cultured in 35-mm glass-bottom dishes (SPL) were treated with the dyes, washed, and visualized using confocal live imaging system (Leica TCS SP5).

Mitochondrial assays

Mitochondrial membrane potential was evaluated in differentiated hNSCs D12 using JC-1 dye. Briefly, cells were incubated in medium containing JC-1 (2.5 μg/ml) and incubated for 10 min at 37°C. Cells were then washed twice with phosphate-buffered saline (PBS). Cells

were counterstained with Hoechst33342 and mounting in PBS for live confocal imaging. JC-1 monomer (green) fluorescence was observed by excitation with the 488-nm laser and emissions from 505 to 530 nm were examined. JC-1 aggregate (red) fluorescence was observed by excitation with the 543-nm laser and emissions over 560 nm were examined. Between 30 and 40 areas were selected randomly from each image from each experiment, and the average intensity of each region was quantified with ImageJ software. The ratio of JC-1 monomers to aggregate intensity was calculated for each region. Values were obtained from three independent experiments.

Mitochondria load was determined by mitochondria copy number. Briefly, total DNA were isolated as previously described (*62*). Two microliters of total DNA (10 ng/μl) was mixed with 0.5 μl of forward and reverse primer mix (10 μM), 7.5 μl of nuclease-free water, and 10 μl of SYBR Green PCR mix (Bio-Rad). The reaction was initiated at 95°C for 5 min, followed by 45 cycles of 95°C for 10 s, 60°C for 10 s, and 72°C for 20 s. Last, melting curve was calculated to confirm the presence of a single PCR product by following these steps: 95°C for 5 s, 66°C for 1 min, and gradual increase in temperature up to 97°C. The mitochondrial DNA (mtDNA) copy number was evaluated based on the ratio of mtDNA to nuclear DNA. The relative amounts of two mtDNA genes (*ND1* and *ND6*) and two nuclear DNA genes (*BECN1* and *NEB*) were measured using qPCR with the primers listed in table S2. mtDNA copy number was obtained by averaging the copy numbers calculated from the set 1 (*ND1*/*BECN1*) pair and set 2 (*ND6*/*NEB*) pair. The individual ratios of set 1 and set 2 were calculated with this formula: $N = 2^{\Delta Cq}$, ΔCq = Cq nDNA − Cq mtDNA.

MitoTimer analysis was performed by transducing hNSCs with lentiviruses carrying mitochondrial-targeting sequences of the human cytochrome *c* oxidase subunit VIII gene fused with a timer-reporter gene. Lentiviral vectors of pMitoTimer were made by modifying pMitoTimer vectors from Addgene (#52659). Briefly, the mitochondrial-targeting sequence of the human cytochrome *c* oxidase subunit VIII (Cox8) gene fused with DsRed1-E5 from the original pMitotimer vector was amplified by PCR with the addition of Nhe I and Sal I restriction sites at 5′ and 3′. The PCR product was then cloned at the multiple cloning site of the modified pCDH-EF1-MCS-T2A-copGFP vector (with the T2A-copGFP sequence removed).

Lysosome assays

$LAMP1^+$ lysosome size measurement was carried out using the analyze-particle function of ImageJ and the "MaxEntropy" threshold. Colocalization of autolysosomal proteins was analyzed using the Coloc2 plugin for ImageJ, Fiji software, and shown as Pearson's coefficients.

GBA activity was measured as described previously (*43*). Briefly, 1 mM 4-MUG (Sigma-Aldrich) in buffer containing 0.25% sodium taurocholate and 0.1 M sodium citrate at pH 5.6 was added to 25 μg of cell lysates to make a total volume of 200 μl. The mixture was then incubated at 37°C for 1 hour. The reaction was stopped by adding 500 μl of 0.1 M glycine (pH 10). Cleaved 4-methylumbelliferone was measured using a SpectraMax Gemini fluorometer (excitation at 365 nm, emission at 445 nm; Molecular Devices, Sunnyvale, CA). GBA2 specific activity was determined in the presence of the GCase 1 inhibitor and conduritol-B-epoxide (CBE, Sigma-Aldrich) (50 μM) for 24 hours. GBA1 specific activity was obtained by subtracting the GBA2 activity level from the total GBA activity. The total GBA activity, GBA1 specific activity, and GBA2 specific activity were measured from the total cell lysates. Lysosomal GBA activity was measured from the lysosome fractions obtained by using a kit from Abcam (ab234047) according to the manufacturer's instruction.

FM 1-43 styryl dye uptake

Cells were washed and incubated in HBSS containing Ca^{2+} for 10 min at 37°C. The buffer was aspirated and then incubated in HBSS with Ca^{2+} containing 60 mM KCl along with FM 1-43FX styryl dye (5 μg/ml) (Thermo Fisher Scientific) for 1 min at 37°C. Cells were then incubated in HBSS with Ca^{2+} containing FM 1-43FX styryl dye (5 μg/ml) for an additional 15 min at 37°C, quickly washed twice with PBS, and incubated overnight at 4°C. The next day, the cells were fixed using 3% PFA for 20 min and mounted in VECTASHIELD medium containing DAPI (Vector Laboratories, West Grove, PA). Images were taken with a confocal microscope.

Chromatin immunoprecipitation–quantitative PCR (ChIP-qPCR)

β-Catenin binding sites were identified as TCF/LEF binding sites using the Jaspar database (http://jaspar.genereg.net) and an 80% score threshold. ChIP assay was carried out as previously described in (*63*). Briefly, chromatin was sheared to an average of 200 to 500 base pairs (bp) using a sonicator (Bioruptor-BMS, Seoul, Korea) and immunoprecipitated using β-catenin antibodies (Abcam, 227499). Immunoprecipitated DNA fragments were collected using magnetic beads (Invitrogen), purified, and subjected to real-time PCR using the primers listed in table S2. The comparative cycle threshold method was used to quantify the results. Data were normalized to the input DNA.

DA release assay

The levels of DA neurotransmitter released from DA neurons were measured in the hMLOs DIV94 and differentiated mDA neuron cultures D15. Media incubated for 2 days were collected and used in DA-level determinations using an ELISA kit (BA E-5300, LDN). In addition, DA release evoked by membrane depolarization was estimated by incubating the cultures (at D15) in fresh N2 media in the presence or absence of 56 mM KCl for 30 min. The evoked DA release was calculated by subtracting the DA release without KCl from the DA level with KCl.

CRISPRi-based gene KD

Lentiviral vectors for knocking down human DNAJC6 were modified from the lenti-EF1a-dCas9-KRAB-Puro vector obtained from Addgene (#99372), with the puromycin cassette replaced by copGFP. The copGFP protein was simultaneously expressed with dCas9 via a self-cleaving 2A peptide (T2A). The sgRNA was designed to target the DNA region from −50 to 300 bp relative to the transcription start site (TSS) of the *DNAJC6* and *LMX1A* genes using the web tool https://portals.broadinstitute.org/gpp/public/analysis-tools/sgrna-design-crisprai. sgRNA cassettes were combined with the U6 promoter by using overlap-extension PCR, with addition of Nhe I and Asc I restriction sites at 5′ and 3′ and cloned at the upstream of EF1-dCAS9-KRAB-CopGFP to generate a U6-hsgDNAJC6- EF1-dCAS9-KRAB-CopGFP vector. For BiFC experiments in KD NSCs, copGFP were removed.

For knocking down mouse Dnajc6, lentiviral vectors were made by making the sgRNA expression vector first. The sgRNA sequence for mouse Dnajc6 was combined with the mU6 promoter from pmU6-gRNA (#53187) from Addgene by using overlap-extension PCR, with the addition of Nhe I and Asc I restriction sites at 5′ and

3′, respectively. Next, mU6-msgDnajc6 was cloned at the upstream of EF1-dCAS9-KRAB-CopGFP to generate mU6-msgDnajc6-EF1-dCAS9-KRAB-CopGFP vector. Two sgRNAs were used at the same time. The sgRNA sequences used in this study are listed in table S3.

CLARITY imaging

For CLARITY imaging, hMLOs were fixed in 4% PFA for 40 min at room temperature and washed three times with 1× PBS with Tween detergent (PBST) and hMLOs blocked in blocking solution (detailed information provided upon request) overnight at room temperature. hMLOs were incubated for 2 nights at room temperature in the blocking solution containing the pSNCA primary antibody (1:300; BioLegend). Secondary antibodies tagged with Cy3 (1:300) and Hoechst were applied at room temperature for 2 nights. Samples were immersed in clearing solution to adjust the refractive index and images were taken with a confocal microscope (Leica TCS SP8). All steps were performed with shaking.

Multielectrode assays

To record the neural activity of the organoids, we used a silicon neural probe with 16 integrated microelectrodes. The width, thickness, and length of the neural probe were 128 μm, 15 μm, and 7 mm, respectively. The impedance of the microelectrodes was 13 ± 1 kilohms at 1 kHz, which was sufficiently low to record neural activity. To insert the neural probe into the organoids and adjust its vertical position, we used a custom microdrive system. We measured the neural signals by inserting the neural probe into the organoid in a culture chamber filled with a culture medium based on DMEM. The organoid with the neural probe was then placed in an incubator, and its neural activity was measured for 10 min using a 16-channel amplifier board (Intan, CA, USA, RHD2132) connected to a data acquisition system (Intan, CA, USA, RHD2000). The sampling rate was 20 kHz per channel, and we used a 300-Hz high-pass filter and a 6-kHz low-pass filter to remove low-frequency signals and high-frequency noise. After recording neural activities, we analyzed the signals using a custom MATLAB sorting code.

RNA-seq analysis

Total RNAs from the H9 hESCs and hMLOs were isolated using TRIzol (Invitrogen) followed by ribosomal RNA removal with a Ribo-Zero Magnetic kit (Epicentre Inc., Madison, WI). Library construction was performed using a Sense mRNA-Seq Library Prep Kit (Lexogen Inc., Vienna, Austria). High-throughput sequencing was performed as paired-end 100 sequencing using a HiSeq 2000 (Illumina, San Diego, CA). RNA-seq reads were mapped using TopHat software to obtain the bam alignment file. Read counts mapped onto transcript regions were extracted from the alignment file using BEDTools (v2.25.0) and R/Bioconductor (version 3.2.2; R Development Core Team, 2011). The alignment file was used to assemble transcripts, estimate their abundances, and detect the differential expression of genes, long intergenic noncoding RNAs, or isoforms. We used fragments per kilobase of exon per million fragments to determine the expression level of gene regions. Global normalization was used for comparisons between samples. Differentially expressed genes between WT and ΔDNAJC6 were defined as genes with absolute log fold changes of normalized read counts greater than 2. Gene classification was based on searches submitted to DAVID (http://david.abcc.ncifcrf.gov/). GO and KEGG pathway analyses were performed using DAVID Bioinformatics Resources version 6.8. Cluster analysis and a heatmap were generated by heatmap.2. R programming language was used to perform all data analysis and generate the figures. Accession number of the RNA-seq data is GSE151190 and can be accessed at Gene Expression Omnibus.

Study approval

Experiments using hESCs/hiPSCs and NSCs derived from mouse embryos were approved by the International Review Board (HYI-15-077-2) and the Institutional Animal Care and Use Committee (IACUC) of Hanyang University (IACUC, 2020-0030A), respectively.

Cell counting and statistical analysis

Total immunoreactive cells were obtained by counting immunopositive cells throughout organoids. hMLOs were cryosectioned as described. Every five sections of organoids were stained and counted for immunopositive cells out of DAPI. An Abercrombie correction factor was applied. In the NSC culture wells (coverslips), immunostained and DAPI-stained cells were counted in 9 to 20 random areas using an eyepiece grid at a magnification of ×200 or ×400, and total positive cells (or percentages) in a well were calculated. Data were obtained from three to five organoids or culture wells (coverslips) in each WT and mutant cell line. For every figure, data are expressed as the means ± SEM and statistical tests are justified as appropriate. Student's *t* tests were applied to compare two groups. Analyses of variance (ANOVAs) were used for comparisons of data with greater than two groups. Post hoc comparisons were performed with a Bonferroni test. A value of $P < 0.05$ was considered significant. Values represent the means ± SEM of the three biological replicates. Significance at $^{*}P < 0.05$; $^{**}P < 0.01$; $^{***}P < 0.001$; n.s., no significance. All statistical analyses were performed using SPSS (Statistics 21; IBM Inc., Bentonville, AR, USA).

SUPPLEMENTARY MATERIALS

Supplementary material for this article is available at http://advances.sciencemag.org/cgi/content/full/7/8/eabb1540/DC1

View/request a protocol for this paper from *Bio-protocol*.

REFERENCES AND NOTES

1. W. Poewe, K. Seppi, C. M. Tanner, G. M. Halliday, P. Brundin, J. Volkmann, A. E. Schrag, A. E. Lang, Parkinson disease. *Nat. Rev. Dis. Primers.* **3**, 17013 (2017).
2. E. Ungewickell, H. Ungewickell, S. E. Holstein, R. Lindner, K. Prasad, W. Barouch, B. Martin, L. E. Greene, E. Eisenberg, Role of auxilin in uncoating clathrin-coated vesicles. *Nature* **378**, 632–635 (1995).
3. S. Edvardson, Y. Cinnamon, A. Ta-Shma, A. Shaag, Y. I. Yim, S. Zenvirt, C. Jalas, S. Lesage, A. Brice, A. Taraboulos, K. H. Kaestner, L. E. Greene, O. Elpeleg, A deleterious mutation in DNAJC6 encoding the neuronal-specific clathrin-uncoating co-chaperone auxilin, is associated with juvenile parkinsonism. *PLOS ONE* **7**, e36458 (2012).
4. C. Koroglu, L. Baysal, M. Cetinkaya, H. Karasoy, A. Tolun, DNAJC6 is responsible for juvenile parkinsonism with phenotypic variability. *Parkinsonism Relat. Disord.* **19**, 320–324 (2013).
5. S. Olgiati, M. Quadri, M. Fang, J. P. Rood, J. A. Saute, H. F. Chien, C. G. Bouwkamp, J. Graafland, M. Minneboo, G. J. Breedveld, J. Zhang; International Parkinsonism Genetics Network, F. W. Verheijen, A. J. Boon, A. J. Kievit, L. B. Jardim, W. Mandemakers, E. R. Barbosa, C. R. Rieder, K. L. Leenders, J. Wang, V. Bonifati, DNAJC6 mutations associated with early-onset Parkinson's disease. *Ann. Neurol.* **79**, 244–256 (2016).
6. Y. I. Yim, T. Sun, L. G. Wu, A. Raimondi, P. De Camilli, E. Eisenberg, L. E. Greene, Endocytosis and clathrin-uncoating defects at synapses of auxilin knockout mice. *Proc. Natl. Acad. Sci. U.S.A.* **107**, 4412–4417 (2010).
7. J. C. Schwamborn, Is Parkinson's disease a neurodevelopmental disorder and will brain organoids help us to understand it? *Stem Cells Dev.* **27**, 968–975 (2018).
8. M. Thiruchelvam, E. K. Richfield, B. M. Goodman, R. B. Baggs, D. A. Cory-Slechta, Developmental exposure to the pesticides paraquat and maneb and the Parkinson's disease phenotype. *Neurotoxicology* **23**, 621–633 (2002).

9. S. Froudist-Walsh, M. A. Bloomfield, M. Veronese, J. Kroll, V. R. Karolis, S. Jauhar, I. Bonoldi, P. K. McGuire, S. Kapur, R. M. Murray, C. Nosarti, O. Howes, The effect of perinatal brain injury on dopaminergic function and hippocampal volume in adult life. *eLife* **6**, e29088 (2017).
10. J. N. Le Grand, L. Gonzalez-Cano, M. A. Pavlou, J. C. Schwamborn, Neural stem cells in Parkinson's disease: A role for neurogenesis defects in onset and progression. *Cell. Mol. Life Sci.* **72**, 773–797 (2015).
11. V. Bonifati, Genetics of Parkinson's disease—State of the art, 2013. *Parkinsonism Relat. Disord.* **20** Suppl 1, S23–S28 (2014).
12. H. Harada, T. Sato, H. Nakamura, Fgf8 signaling for development of the midbrain and hindbrain. *Dev. Growth Differ.* **58**, 437–445 (2016).
13. J. Yang, A. Brown, D. Ellisor, E. Paul, N. Hagan, M. Zervas, Dynamic temporal requirement of *Wnt1* in midbrain dopamine neuron development. *Development* **140**, 1342–1352 (2013).
14. R. D. Bayly, C. Y. Brown, S. Agarwala, A novel role for FOXA2 and SHH in organizing midbrain signaling centers. *Dev. Biol.* **369**, 32–42 (2012).
15. S. Chung, A. Leung, B. S. Han, M. Y. Chang, J. I. Moon, C. H. Kim, S. Hong, J. Pruszak, O. Isacson, K. S. Kim, Wnt1-lmx1a forms a novel autoregulatory loop and controls midbrain dopaminergic differentiation synergistically with the SHH-FoxA2 pathway. *Cell Stem Cell* **5**, 646–658 (2009).
16. T. Nakatani, M. Kumai, E. Mizuhara, Y. Minaki, Y. Ono, Lmx1a and Lmx1b cooperate with Foxa2 to coordinate the specification of dopaminergic neurons and control of floor plate cell differentiation in the developing mesencephalon. *Dev. Biol.* **339**, 101–113 (2010).
17. S. H. Yi, X. B. He, Y. H. Rhee, C. H. Park, T. Takizawa, K. Nakashima, S. H. Lee, Foxa2 acts as a co-activator potentiating expression of the Nurr1-induced DA phenotype via epigenetic regulation. *Development* **141**, 761–772 (2014).
18. M. Decressac, N. Volakakis, A. Bjorklund, T. Perlmann, NURR1 in Parkinson disease—From pathogenesis to therapeutic potential. *Nat. Rev. Neurol.* **9**, 629–636 (2013).
19. E. Arenas, Foxa2: The rise and fall of dopamine neurons. *Cell Stem Cell* **2**, 110–112 (2008).
20. H. Rekaik, F. X. Blaudin de The, J. Fuchs, O. Massiani-Beaudoin, A. Prochiantz, R. L. Joshi, Engrailed homeoprotein protects mesencephalic dopaminergic neurons from oxidative stress. *Cell Rep.* **13**, 242–250 (2015).
21. H. Doucet-Beaupre, C. Gilbert, M. S. Profes, A. Chabrat, C. Pacelli, N. Giguere, V. Rioux, J. Charest, Q. Deng, A. Laguna, J. Ericson, T. Perlmann, S. L. Ang, F. Cicchetti, M. Parent, L. E. Trudeau, M. Levesque, Lmx1a and Lmx1b regulate mitochondrial functions and survival of adult midbrain dopaminergic neurons. *Proc. Natl. Acad. Sci. U.S.A.* **113**, E4387–E4396 (2016).
22. A. Laguna, N. Schintu, A. Nobre, A. Alvarsson, N. Volakakis, J. K. Jacobsen, M. Gomez-Galan, E. Sopova, E. Joodmardi, T. Yoshitake, Q. Deng, J. Kehr, J. Ericson, P. Svenningsson, O. Shupliakov, T. Perlmann, Dopaminergic control of autophagic-lysosomal function implicates Lmx1b in Parkinson's disease. *Nat. Neurosci.* **18**, 826–835 (2015).
23. D. Alvarez-Fischer, J. Fuchs, F. Castagner, O. Stettler, O. Massiani-Beaudoin, K. L. Moya, C. Bouillot, W. H. Oertel, A. Lombes, W. Faigle, R. L. Joshi, A. Hartmann, A. Prochiantz, Engrailed protects mouse midbrain dopaminergic neurons against mitochondrial complex I insults. *Nat. Neurosci.* **14**, 1260–1266 (2011).
24. B. Kadkhodaei, A. Alvarsson, N. Schintu, D. Ramskold, N. Volakakis, E. Joodmardi, T. Yoshitake, J. Kehr, M. Decressac, A. Bjorklund, R. Sandberg, P. Svenningsson, T. Perlmann, Transcription factor Nurr1 maintains fiber integrity and nuclear-encoded mitochondrial gene expression in dopamine neurons. *Proc. Natl. Acad. Sci. U.S.A.* **110**, 2360–2365 (2013).
25. Y. X. Yang, D. S. Latchman, Nurr1 transcriptionally regulates the expression of α-synuclein. *Neuroreport* **19**, 867–871 (2008).
26. H. Liu, L. Wei, Q. Tao, H. Deng, M. Ming, P. Xu, W. Le, Decreased NURR1 and PITX3 gene expression in Chinese patients with Parkinson's disease. *Eur. J. Neurol.* **19**, 870–875 (2012).
27. W. D. Le, P. Xu, J. Jankovic, H. Jiang, S. H. Appel, R. G. Smith, D. K. Vassilatis, Mutations in NR4A2 associated with familial Parkinson disease. *Nat. Genet.* **33**, 85–89 (2003).
28. J. Wen, S. Brogna, Nonsense-mediated mRNA decay. *Biochem. Soc. Trans.* **36**, 514–516 (2008).
29. S. H. Ramirez, S. Fan, H. Dykstra, S. Rom, A. Mercer, N. L. Reichenbach, L. Gofman, Y. Persidsky, Inhibition of glycogen synthase kinase 3β promotes tight junction stability in brain endothelial cells by half-life extension of occludin and claudin-5. *PLOS ONE* **8**, e55972 (2013).
30. M. T. Alves dos Santos, M. P. Smidt, En1 and Wnt signaling in midbrain dopaminergic neuronal development. *Neural Dev.* **6**, 23 (2011).
31. H. X. Hao, Y. Xie, Y. Zhang, O. Charlat, E. Oster, M. Avello, H. Lei, C. Mickanin, D. Liu, H. Ruffner, X. Mao, Q. Ma, R. Zamponi, T. Bouwmeester, P. M. Finan, M. W. Kirschner, J. A. Porter, F. C. Serluca, F. Cong, ZNRF3 promotes Wnt receptor turnover in an R-spondin-sensitive manner. *Nature* **485**, 195–200 (2012).
32. L. Brunt, S. Scholpp, The function of endocytosis in Wnt signaling. *Cell. Mol. Life Sci.* **75**, 785–795 (2018).
33. J. Y. Kim, J. S. Lee, H. S. Hwang, D. R. Lee, C. Y. Park, S. J. Jung, Y. R. You, D. S. Kim, D. W. Kim, Wnt signal activation induces midbrain specification through direct binding of the beta-catenin/TCF4 complex to the EN1 promoter in human pluripotent stem cells. *Exp. Mol. Med.* **50**, 24 (2018).
34. M. Joksimovic, R. Awatramani, Wnt/β-catenin signaling in midbrain dopaminergic neuron specification and neurogenesis. *J. Mol. Cell Biol.* **6**, 27–33 (2014).
35. C. H. Yan, M. Levesque, S. Claxton, R. L. Johnson, S. L. Ang, Lmx1a and lmx1b function cooperatively to regulate proliferation, specification, and differentiation of midbrain dopaminergic progenitors. *J. Neurosci.* **31**, 12413–12425 (2011).
36. D. Gyllborg, M. Ahmed, E. M. Toledo, S. Theofilopoulos, S. Yang, C. Ffrench-Constant, E. Arenas, The matricellular protein R-spondin 2 promotes midbrain dopaminergic neurogenesis and differentiation. *Stem Cell Rep.* **11**, 651–664 (2018).
37. E. J. Hoekstra, L. von Oerthel, L. P. van der Heide, W. M. Kouwenhoven, J. V. Veenvliet, I. Wever, Y. R. Jin, J. K. Yoon, A. J. van der Linden, F. C. Holstege, M. J. Groot Koerkamp, M. P. Smidt, *Lmx1a* encodes a rostral set of mesodiencephalic dopaminergic neurons marked by the *Wnt*/B-catenin signaling activator *R-spondin* 2. *PLOS ONE* **8**, e74049 (2013).
38. J. Jo, Y. Xiao, A. X. Sun, E. Cukuroglu, H. D. Tran, J. Goke, Z. Y. Tan, T. Y. Saw, C. P. Tan, H. Lokman, Y. Lee, D. Kim, H. S. Ko, S. O. Kim, J. H. Park, N. J. Cho, T. M. Hyde, J. E. Kleinman, J. H. Shin, D. R. Weinberger, E. K. Tan, H. S. Je, H. H. Ng, Midbrain-like organoids from human pluripotent stem cells contain functional dopaminergic and neuromelanin-producing neurons. *Cell Stem Cell* **19**, 248–257 (2016).
39. N. Prakash, W. Wurst, Genetic networks controlling the development of midbrain dopaminergic neurons. *J. Physiol.* **575**, 403–410 (2006).
40. M. Subramaniam, D. Althof, S. Gispert, J. Schwenk, G. Auburger, A. Kulik, B. Fakler, J. Roeper, Mutant α-synuclein enhances firing frequencies in dopamine substantia nigra neurons by oxidative impairment of A-type potassium channels. *J. Neurosci.* **34**, 13586–13599 (2014).
41. B. C. Sun, K. X. Huang, G. Z. Jin, Repeated reserpine treatment alters firing pattern and responses of substantia nigral dopamine neurons. *Eur. J. Pharmacol.* **231**, 331–338 (1993).
42. S. Robinson, D. M. Smith, S. J. Mizumori, R. D. Palmiter, Firing properties of dopamine neurons in freely moving dopamine-deficient mice: Effects of dopamine receptor activation and anesthesia. *Proc. Natl. Acad. Sci. U.S.A.* **101**, 13329–13334 (2004).
43. E. J. Bae, N. Y. Yang, M. Song, C. S. Lee, J. S. Lee, B. C. Jung, H. J. Lee, S. Kim, E. Masliah, S. P. Sardi, S. J. Lee, Glucocerebrosidase depletion enhances cell-to-cell transmission of α-synuclein. *Nat. Commun.* **5**, 4755 (2014).
44. A. R. Esteves, D. M. Arduino, D. F. Silva, C. R. Oliveira, S. M. Cardoso, Mitochondrial dysfunction: The road to alpha-synuclein oligomerization in PD. *Parkinson's Dis.* **2011**, 693761 (2011).
45. R. C. Laker, P. Xu, K. A. Ryall, A. Sujkowski, B. M. Kenwood, K. H. Chain, M. Zhang, M. A. Royal, K. L. Hoehn, M. Driscoll, P. N. Adler, R. J. Wessells, J. J. Saucerman, Z. Yan, A novel *MitoTimer* reporter gene for mitochondrial content, structure, stress, and damage in vivo. *J. Biol. Chem.* **289**, 12005–12015 (2014).
46. S. Sato, T. Uchihara, T. Fukuda, S. Noda, H. Kondo, S. Saiki, M. Komatsu, Y. Uchiyama, K. Tanaka, N. Hattori, Loss of autophagy in dopaminergic neurons causes Lewy pathology and motor dysfunction in aged mice. *Sci. Rep.* **8**, 2813 (2018).
47. P. W.-L. Ho, C.-T. Leung, H. Liu, S. Y.-Y. Pang, C. S.-C. Lam, J. Xian, L. Li, M. H.-W. Kung, D. B. Ramsden, S.-L. Ho, Age-dependent accumulation of oligomeric SNCA/α-synuclein from impaired degradation in mutant LRRK2 knockin mouse model of Parkinson disease: Role for therapeutic activation of chaperone-mediated autophagy (CMA). *Autophagy* **16**, 347–370 (2019).
48. P. P. Y. Lie, R. A. Nixon, Lysosome trafficking and signaling in health and neurodegenerative diseases. *Neurobiol. Dis.* **122**, 94–105 (2019).
49. I. Stojkovska, D. Krainc, J. R. Mazzulli, Molecular mechanisms of α-synuclein and GBA1 in Parkinson's disease. *Cell Tissue Res.* **373**, 51–60 (2018).
50. L. F. Burbulla, S. Jeon, J. Zheng, P. Song, R. B. Silverman, D. Krainc, A modulator of wild-type glucocerebrosidase improves pathogenic phenotypes in dopaminergic neuronal models of Parkinson's disease. *Sci. Transl. Med.* **11**, eaau6870 (2019).
51. S. Y. Yang, M. Gegg, D. Chau, A. Schapira, Glucocerebrosidase activity, cathepsin D and monomeric α-synuclein interactions in a stem cell derived neuronal model of a PD associated GBA1 mutation. *Neurobiol. Dis.* **134**, 104620 (2020).
52. J. R. Mazzulli, Y. H. Xu, Y. Sun, A. L. Knight, P. J. McLean, G. A. Caldwell, E. Sidransky, G. A. Grabowski, D. Krainc, Gaucher disease glucocerebrosidase and α-synuclein form a bidirectional pathogenic loop in synucleinopathies. *Cell* **146**, 37–52 (2011).
53. J. R. Mazzulli, F. Zunke, O. Isacson, L. Studer, D. Krainc, α-Synuclein-induced lysosomal dysfunction occurs through disruptions in protein trafficking in human midbrain synucleinopathy models. *Proc. Natl. Acad. Sci. U.S.A.* **113**, 1931–1936 (2016).
54. M. H. Larson, L. A. Gilbert, X. Wang, W. A. Lim, J. S. Weissman, L. S. Qi, CRISPR interference (CRISPRi) for sequence-specific control of gene expression. *Nat. Protoc.* **8**, 2180–2196 (2013).

55. S. Saxena, P. Caroni, Selective neuronal vulnerability in neurodegenerative diseases: From stressor thresholds to degeneration. *Neuron* **71**, 35–48 (2011).
56. L. Yu, C. K. McPhee, L. Zheng, G. A. Mardones, Y. Rong, J. Peng, N. Mi, Y. Zhao, Z. Liu, F. Wan, D. W. Hailey, V. Oorschot, J. Klumperman, E. H. Baehrecke, M. J. Lenardo, Termination of autophagy and reformation of lysosomes regulated by mTOR. *Nature* **465**, 942–946 (2010).
57. Y. Rong, M. Liu, L. Ma, W. Du, H. Zhang, Y. Tian, Z. Cao, Y. Li, H. Ren, C. Zhang, L. Li, S. Chen, J. Xi, L. Yu, Clathrin and phosphatidylinositol-4,5-bisphosphate regulate autophagic lysosome reformation. *Nat. Cell Biol.* **14**, 924–934 (2012).
58. S. Mullin, A. Schapira, α-Synuclein and mitochondrial dysfunction in Parkinson's disease. *Mol. Neurobiol.* **47**, 587–597 (2013).
59. D. Sulzer, Multiple hit hypotheses for dopamine neuron loss in Parkinson's disease. *Trends Neurosci.* **30**, 244–250 (2007).
60. C. S. Chan, T. S. Gertler, D. J. Surmeier, Calcium homeostasis, selective vulnerability and Parkinson's disease. *Trends Neurosci.* **32**, 249–256 (2009).
61. M. A. Lancaster, M. Renner, C. A. Martin, D. Wenzel, L. S. Bicknell, M. E. Hurles, T. Homfray, J. M. Penninger, A. P. Jackson, J. A. Knoblich, Cerebral organoids model human brain development and microcephaly. *Nature* **501**, 373–379 (2013).
62. W. Guo, L. Jiang, S. Bhasin, S. M. Khan, R. H. Swerdlow, DNA extraction procedures meaningfully influence qPCR-based mtDNA copy number determination. *Mitochondrion* **9**, 261–265 (2009).
63. N. Wulansari, E. H. Kim, Y. A. Sulistio, Y. H. Rhee, J. J. Song, S. H. Lee, Vitamin C-induced epigenetic modifications in donor NSCs establish midbrain marker expressions critical for cell-based therapy in Parkinson's disease. *Stem Cell Rep.* **9**, 1192–1206 (2017).

Acknowledgments: We thank Shim Sung Han and Min Yeon Go for helpful assistance. **Funding:** This work was supported by the grants 2017R1A5A2015395, 2017M3A9B4062415, and 2020M3A9D8039925 (to S.-H.L.); NRF-2018R1A5A2025964 (to S.-J.L); and NRF-2020R1I1A1A01072544 (to N.W.) funded by the National Research Foundation of Korea (NRF) of the Ministry of Science and ICT, Republic of Korea. **Author contributions:** Conception and design, collection and/or data assembly, data analysis and interpretation, manuscript writing, and final approval of manuscript: N.W.; collection and/or data assembly, data analysis and interpretation, and manuscript writing: W.H.W.D.; collection and/or data assembly: H.-J.W., M.-Y.C., J.K., E.-J.B., W.S., J.-H.L., I.-J.C., and H.S.; conception and design, financial support, administrative support, provision of study material, data analysis and interpretation, manuscript writing, and final approval of manuscript: S.-J.L. and S.-H.L. **Competing interests:** The authors declare that they have no competing interests. **Data and materials availability:** All data needed to evaluate the conclusions in the paper are present in the paper and/or the Supplementary Materials. Additional data related to this paper may be requested from the authors.

Submitted 3 February 2020
Accepted 28 December 2020
Published 17 February 2021
10.1126/sciadv.abb1540

Citation: N. Wulansari, W. H. W. Darsono, H.-J. Woo, M.-Y. Chang, J. Kim, E.-J. Bae, W. Sun, J.-H. Lee, I.-J. Cho, H. Shin, S.-J. Lee, S.-H. Lee, Neurodevelopmental defects and neurodegenerative phenotypes in human brain organoids carrying Parkinson's disease-linked *DNAJC6* mutations. *Sci. Adv.* **7**, eabb1540 (2021).